

1 Differential response of a tree-killing bark beetle to forest structure 2 and composition across a gradient of climatic water deficit

3 Michael J. Koontz^{1,2,3*}, Andrew M. Latimer^{1,2}, Leif A. Mortenson⁴, Christopher J. Fettig⁵, Malcolm P.
4 North^{1,2,6}

5 ¹Graduate Group in Ecology, University of California, Davis, CA, USA

6 ²Department of Plant Sciences, University of California, Davis, CA, USA

7 ³Earth Lab, University of Colorado-Boulder; Boulder, CO, USA

8 ⁴USDA Forest Service, Pacific Southwest Research Station, Placerville, CA, USA

9 ⁵USDA Forest Service, Pacific Southwest Research Station, Davis, CA, USA

10 ⁶USDA Forest Service, Pacific Southwest Research Station, Mammoth Lakes, CA, USA

11 *Correspondence: michael.koontz@colorado.edu

12 *Keywords:* bark beetles, forest structure, drones, climatic water deficit, Sierra Nevada, California, disturbance,
13 structure from motion, *Dendroctonus brevicomis*, *Pinus ponderosa*, threshold dynamics

14 Date report generated: August 01, 2019

15 Abstract

16 The Californian hot drought of 2012 to 2015 created favorable conditions for unprecedented ponderosa pine
17 (*Pinus ponderosa*) mortality in the Sierra Nevada mountain range, largely caused by the western pine beetle
18 (*Dendroctonus brevicomis*). Climate conditions related to tree water stress as well as forest structure and
19 composition can influence the severity of forest insect disturbance, but it remains challenging to consider how
20 these variables may interact to produce patterns of tree mortality. Previous studies have shown an interaction
21 between climate conditions and forest density in their effect on tree mortality, but density is a coarse gauge
22 of forest structure that can affect western pine beetle behavior in a number of ways. Measuring broad-scale
23 climate conditions simultaneously with complex forest structure– including tree species, tree size, and local
24 density– will refine our understanding of how these variables interact, but is generally expensive and/or
25 labor-intensive. We overcame these hurdles using aerial drone surveys over an established network of 160
26 forest plots along a 350km and 1000m elevation gradient in western slope Sierra ponderosa pine/mixed-conifer
27 forests. Using Structure from Motion (SfM) processing on over 450,000 images and field measurements from
28 the coincident ground plots, we determined tree size, location, and species for individual trees over 9km² of
29 forest that experienced ponderosa pine mortality as a result of western pine beetle colonization. We modeled

30 the probability of ponderosa pine mortality as a linear combination of forest structure variables and site-level
31 climatic water deficit, and used a Gaussian process to estimate the spatial covariance in the response.

32 We found that greater host density strongly increased the probability of host mortality, and greater host
33 size generally decreased the probability of host mortality. There was also a strong three-way interaction
34 between host density, host size, and climatic water deficit such that host density and host size tended to
35 synergistically increase the probability of host mortality at hot/dry sites, but denser, smaller trees tended to
36 drive mortality in cool/wet sites.

37 Our results demonstrate a variable response of the western pine beetle to complex forest structure and
38 composition across an environmental gradient during the same hot drought, which may indicate forest sites
39 were in different stages of disturbance (from “endemic” to “outbreak”) depending on their regional climate.
40 Management interventions that reduce host density may decrease the probability of tree mortality attributed
41 to western pine beetles in the future, and our results suggest that focusing these treatments on areas that are
42 most likely to exceed feedback thresholds (i.e., hot/dry sites with many available hosts) will have the best
43 chance of increasing tree survivorship, specifically of larger trees.

44 Introduction

45 Bark beetles dealt the final blow to many of the nearly 150 million trees killed in the California hot drought of
46 2012 to 2015 and its aftermath (USDAFS 2019). A harbinger of climate change effects to come, record high
47 temperatures exacerbated the drought (Griffin and Anchukaitis 2014), which increased water stress on trees
48 (Asner et al. 2016), making them more susceptible to colonization by bark beetles (Fettig 2012, Kolb et al.
49 2016). A century of fire suppression policy has enabled forests to grow into dense stands, which also makes
50 them more vulnerable to bark beetles (Fettig 2012). This combination of environmental conditions and forest
51 structural characteristics led to tree mortality events of unprecedented size in the driest, densest forests across
52 the state (Young et al. 2017). The mechanisms underlying the link between tree susceptibility to colonization
53 by insects and hot, dry conditions are often directly attributed to tree physiology (Bentz et al. 2010), while
54 the link to forest density is multifaceted (Fettig 2012). Because forest density is a coarse metric of the complex
55 forest structure to which bark beetles respond (Raffa et al. 2008), our understanding of the connection
56 between forest density and insect disturbance severity could be enhanced with more finely-resolved measures
57 of forest structure, such as tree size, tree species, and local tree density within a forest stand (Stephenson
58 et al. 2019, Fettig et al. 2019). Further, the interaction between local-scale complex forest structure and
59 broad-scale environmental conditions as they affect forest insect disturbance remains underexplored (Seidl et
60 al. 2016, Stephenson et al. 2019, Fettig et al. 2019).

61 The ponderosa pine/mixed-conifer forests in California's Sierra Nevada region are characterized by regular
62 bark beetle disturbances, primarily by the influence of western pine beetle (*Dendroctonus brevicomis*; WPB)
63 on its host ponderosa pine (*Pinus ponderosa*), although several species are of importance (Fettig 2016).
64 The WPB is a "primary" bark beetle, with its reproductive success contingent upon enough beetles "mass
65 attacking" the host tree, overwhelming its defenses, and causing tree mortality (Raffa and Berryman 1983).
66 This Allee effect creates a strong coupling between beetle host selection behavior and host tree susceptibility
67 to colonization (Raffa and Berryman 1983, Logan et al. 1998). Under normal conditions, weakened trees are
68 the most susceptible to colonization and will be the main targets of aggressive bark beetles like the western
69 pine beetle (Bentz et al. 2010, Raffa et al. 2015). A key defense mechanism of trees to bark beetle attack is
70 to flood beetle bore holes with resin, which physically expels beetles and may interrupt beetle communication
71 (Franceschi et al. 2005, Raffa et al. 2015). Under severe water stress, trees no longer have the resources
72 available to mount this defense (Kolb et al. 2016) and thus prolonged drought can often trigger increased
73 bark beetle-induced tree mortality as average tree vigor declines (Bentz et al. 2010). As local population
74 density of beetles increases due to successful reproduction within spatially-aggregated weakened trees, as
75 might occur during severe drought, mass attacks become capable of overwhelming many tree's defenses and
76 even healthy trees may be susceptible to colonization and mortality (Bentz et al. 2010, Raffa et al. 2015).
77 Thus, water stress can be a key determinant of whether individual trees are susceptible to bark beetles under
78 many conditions, and this environmental condition may interact with other forest features, such as tree size,
79 to drive susceptibility under extreme conditions (Bentz et al. 2010, Stephenson et al. 2019).

80 Forest structure— the spatial distribution and size of trees— and species composition, also strongly influence
81 WPB activity. For instance, high-density forests are more prone to bark beetle-induced tree mortality, and
82 several mechanisms likely underlie this phenomenon (Fettig 2012). For example, a high-density forest may
83 experience greater bark beetle-induced tree mortality for several reasons including: a) host availability is
84 high and shorter dispersal distances facilitate successful colonization of those hosts (Miller and Keen 1960,
85 Berryman 1982, Fettig et al. 2007); b) high host availability reduces the chance of individual beetles wasting
86 their limited resources flying to and landing on a non-host tree (Moeck et al. 1981, Evenden et al. 2014); c)
87 crowded trees experience greater competition for water resources and thus average tree resistance is lower
88 (Hayes et al. 2009); or d) smaller gaps between trees protect pheromone plumes from dissipation by the wind
89 and thus enhance intraspecific beetle communication (Thistle et al. 2004). Additionally, tree size affects bark
90 beetle host selection behavior as smaller trees tend to have less capacity for resisting attack, but larger trees
91 represent a more desirable target because their thicker phloem provides greater nutritional content (Chubaty
92 et al. 2009, Graf et al. 2012). Tree density and host density thus paint a fundamentally limited picture of

93 the mechanism by which forest structure and composition affect bark beetle disturbance, but finer-grain
94 information explicitly recognizing tree size, species composition (e.g., host versus non-host composition), and
95 local tree density should more appropriately capture the ecological processes underlying insect-induced tree
96 mortality. Additionally, considering the effects of complex forest structure simultaneously to the effects of
97 environmental conditions may help refine our understanding of observed patterns of tree mortality in the
98 recent California hot drought.

99 The vast spatial extent of tree mortality in the 2012 to 2015 California hot drought (USDAFS 2019) challenges
100 our ability to simultaneously consider how broad-scale environmental conditions may interact with local,
101 complex forest structure to affect the dynamic between bark beetle host selection and host tree susceptibility
102 to attack (Anderegg et al. 2015, Stephenson et al. 2019). Measuring complex forest structure generally
103 requires expensive instrumentation (Kane et al. 2014, Asner et al. 2016) or labor-intensive field surveys
104 (Larson and Churchill 2012, Stephenson et al. 2019), which constrains survey extent and frequency. Small,
105 unhumanned aerial systems (sUAS) enable relatively fast and cheap remote imaging over dozens of hectares of
106 forest, which can be used to measure complex forest structure at the individual tree scale (Morris et al. 2017,
107 Shiklomanov et al. 2019). Distributing such surveys across an environmental gradient is a viable approach to
108 overcoming the data acquisition challenge inherent in investigating phenomena with both a strong local- and
109 a strong broad-scale component.

110 We used ultra-high resolution, drone-derived remote sensing data over a network of 32 sites in Sierra Nevada
111 yellow pine/mixed-conifer forests spanning 1000m of elevation and 350km of latitude and covering a total of
112 9 square kilometers to ask how broad-scale environmental conditions interacted with local, complex forest
113 structure to affect the probability of tree mortality during the cumulative tree mortality event of 2012 to
114 2018. We asked:

- 115 1. How does host tree density and average host tree size affect the severity of western pine beetle
116 disturbance?
- 117 2. How does tree density of all species (hereafter “overall density”) and average tree size of all species
118 (hereafter “overall size”) affect the severity of western pine beetle disturbance?
- 119 3. How does environmentally-driven tree moisture stress affect the severity of western pine beetle distur-
120 bance?
- 121 4. Do the effects of forest structure and environmental condition on western pine beetle disturbance
122 interact?

¹²³ **Methods**

¹²⁴ **Study system**

¹²⁵ The study sites were chosen to reflect typical west-side Sierra Nevada yellow pine/mixed-conifer forests and
¹²⁶ were dominated by ponderosa pine trees, *Pinus ponderosa* (Fettig et al. 2019), whose primary bark beetle
¹²⁷ predator in California is the western pine beetle (WPB), *Dendroctonus brevicomis*. The typical life cycle
¹²⁸ of WPBs consists of pioneer beetles dispersing to a new host tree, determining the host's susceptibility to
¹²⁹ attack, and using pheromone signals to attract other WPBs. The attracted WPBs mass attack the tree by
¹³⁰ boring into its inner bark, laying eggs, and dying, leaving their offspring to develop inside the doomed tree
¹³¹ before themselves dispersing to a new potential host (Raffa et al. 2008). In California, the WPB can have 2-3
¹³² generations in a single year and can often out-compete its congener, the mountain pine beetle, *Dendroctonus*
¹³³ *ponderosa* (MPB), for the ponderosa pine host (Fettig et al. 2019).

¹³⁴ We built our study on 180 vegetation/forest insect monitoring plots at 36 sites established between 2016
¹³⁵ and 2017 by Fettig et al. (2019) (Figure 1). These established plots were located in WPB-attacked, yellow
¹³⁶ pine/mixed-conifer forests across the Eldorado, Stanislaus, Sierra and Sequoia National Forests and were
¹³⁷ stratified by elevation (914-1219 meters [3000-4000 feet], 1219-1524 meters [4000-5000 feet], 1524-1828 meters
¹³⁸ [5000-6000 feet] above sea level). In the Sequoia National Forest, the southernmost National Forest in our
¹³⁹ study, plots were stratified with the lowest elevation band between 1219 and 1524 meters (4000-5000 feet) and
¹⁴⁰ extended to an upper elevation band of 1828-2133 meters (6000-7000 feet) to capture a more similar forest
¹⁴¹ community composition as at the more northern National Forests. The sites have variable forest structure
¹⁴² and plot locations were selected in areas with >40% ponderosa pine basal area and >10% ponderosa pine
¹⁴³ mortality. At each site, five 0.04 ha circular plots were installed along transects with between 80 and 200m
¹⁴⁴ between each plot. In the field, Fettig et al. (2019) mapped all stem locations relative to the center of each
¹⁴⁵ plot using azimuth/distance measurements. Tree identity to species, tree height, and diameter at breast
¹⁴⁶ height (DBH) were recorded if DBH was greater than 6.35cm. Year of mortality was estimated based on
¹⁴⁷ needle color and retention, if it wasn't directly observed between site visits. A small section of bark was
¹⁴⁸ removed from dead trees to confirm insect activity. During the spring and early summer of 2018, all field
¹⁴⁹ plots were revisited to assess whether dead trees had fallen (Fettig et al. 2019).

¹⁵⁰ **Instrumentation**

¹⁵¹ Imagery was captured using a DJI Zenmuse X3 RGB camera (DJI 2015a) and a Micasense RedEdge3 5-band
¹⁵² multispectral camera (Micasense 2015). We mounted both of these instruments simultaneously on a DJI
¹⁵³ Matrice 100 aircraft (DJI 2015b) using the DJI 3-axis stabilized gimbal for the Zenmuse X3 camera and a

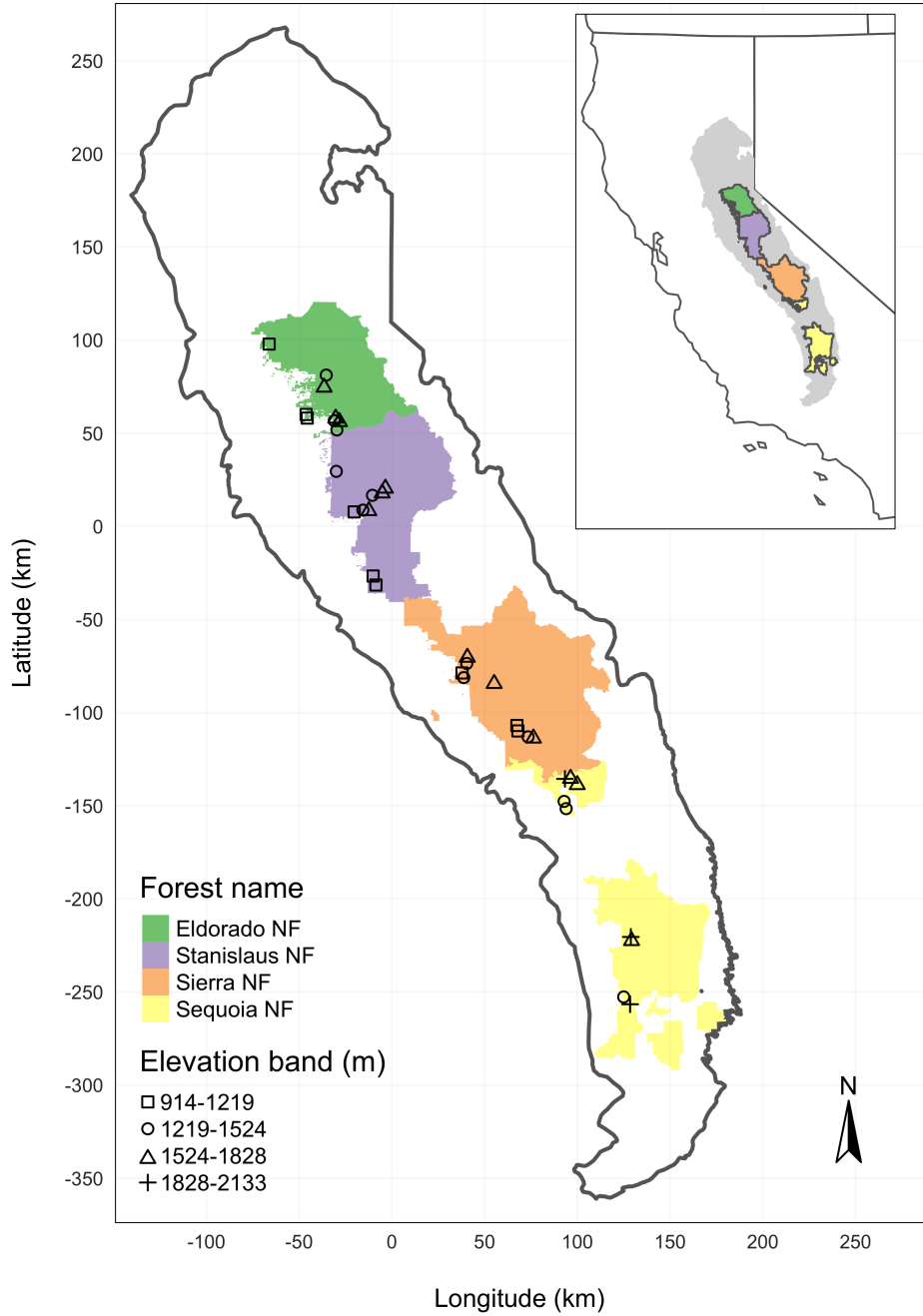


Figure 1: The network of field plots spanned a 350 km latitudinal gradient from the Eldorado National Forest in the north to the Sequoia National Forest in the south. Plots were stratified by three elevation bands in each forest, with the plots in the Sequoia National Forest (the southern-most National Forest) occupying elevation bands 305m above the three bands in the other National Forests in order to capture a similar community composition.

154 Micasense angled fixed mount for the RedEdge3 camera. The gimbal and the angled fixed mount ensured
155 both instruments were nadir-facing during image capture. Just prior to or after image capture at each site,
156 we calibrated the RedEdge3 camera by taking an image of a calibration panel on the ground in full sun with
157 known reflectance values for each of the 5 narrow bands (Table 1).

Table 1: Reflectance sensitivity of the Micasense Rededge3 camera. The calibration panel value represents the reflectance of the calibration panel for the given wavelength.

Band number	Band name	Center wavelength	Band width	Wavelength range	Panel reflectance
1	blue (b)	475	20	465-485	0.64
2	green (g)	560	20	550-570	0.64
3	red (r)	668	10	663-673	0.64
4	near infrared (nir)	840	40	820-860	0.6
5	red edge (re)	717	10	712-722	0.63

158 Flight protocol

159 Image capture was conducted as close to solar noon as possible to minimize shadow effects (varying primarily
160 due to site accessibility; always within 4 hours, usually within 2 hours). Prior to the aerial survey, two strips
161 of bright orange drop cloth (~100cm x 15cm) were positioned as an “X” over the permanent monuments
162 marking the center of the 5 field plots from Fettig et al. (2019).

163 For each of the 36 sites (containing 5 plots each), we captured imagery over the surrounding ~40 hectares of
164 forested area using north-south aerial transects. For three sites, we surveyed less surrounding area in order to
165 maintain visual and radio communication with the aircraft during flight which can be obstructed by rolling
166 terrain or non-centrally available takeoff locations.

167 We preprogrammed aerial transects using Map Pilot for DJI on iOS flight software (hereafter Map Pilot)
168 (DronesMadeEasy 2018). Using the Map Pilot software, we included an altitude adjustment along each
169 aerial transect using a 1-arc-second digital elevation model (Farr et al. 2007) such that the aircraft’s altitude
170 remained approximately constant at 120 meters above ground level in order to maintain consistent ground
171 sampling distance (centimeters on the ground per pixel) in the imagery. Ground sampling distance was
172 approximately 5 cm/px for the Zenmuse X3 RGB camera and approximately 8 cm/px for the RedEdge3
173 multispectral camera. For this analysis, we dropped 4 sites whose imagery was of insufficient quality to
174 process.

175 Structure from motion (SfM) processing requires highly overlapping images, especially in densely vegetated
176 areas (Frey et al. 2018). We planned transects with 90% forward overlap and 90% side overlap at 100 meters
177 below the lens. Thus, with flights being at 120 meters above ground level, we achieved slightly higher than
178 90/90% overlap for objects under 20 meters tall (91.6/91.6% overlap at the ground). Overlap values were
179 based on focal length (3.6mm), sensor width (6.2mm), and image dimension (4000x3000 pixels) parameters
180 of the Zenmuse X3 camera. Images were captured at a constant rate of 1 image every 2 seconds for both
181 cameras. A forward overlap of 90% at 100 meters translates to a flight speed of approximately 6.45 m/s and
182 a side overlap of 90% at 100 meters translates to transects approximately 17.2 meters apart. The RedEdge3
183 camera has a different focal length (5.4mm), sensor width (4.8mm), and image dimension (1280x960 pixels),
184 which translates to image overlap of 80.7/80.7 % at 100m below the lens and 83.9/83.9 % at ground level.
185 Approximately 1900 photos were captured over each 40 hectare survey area for each camera.

186 **Structure from Motion (SfM) processing**

187 We used structure from motion (SfM) to generate dense point clouds (Figure 2), digital surface models
188 (Figure 3), and orthorectified reflectance maps (Figure 4) for each field site (Frey et al. 2018). We used
189 Pix4Dmapper Cloud to process imagery using parameters ideal for images of a densely vegetated area taken
190 by a multispectral camera. For 29 sites, we processed the RedEdge3 multispectral imagery alone. For three
191 sites, we processed the RGB and the multispectral imagery in the same project to enhance the point density
192 of the resulting point cloud. All SfM projects resulted in a single processing “block,” indicating that all
193 images in the project were optimized and processed together.

194 **Creating canopy height models**

195 We classified each survey area’s dense point cloud into “ground” and “non-ground” points using a cloth
196 simulation filter algorithm (Zhang et al. 2016) implemented in the `lidR` (Roussel et al. 2019) package. We
197 rasterized the ground points using the `raster` package (Hijmans et al. 2019) to create a digital terrain model
198 (Figure 5) representing the ground underneath the vegetation at 1 meter resolution. We created a canopy
199 height model (Figure 6) by subtracting the digital terrain model from the digital surface model created in
200 Pix4Dmapper.

201 **Tree detection**

202 We tested a total of 7 automatic tree detection algorithms and a total of 177 parameter sets on the canopy
203 height model or the dense point cloud to locate trees within each site (Table 2). We used 3 parameter sets of
204 a variable window filter using the `vwf()` function in the `ForestTools` (Plowright 2018) R package, including

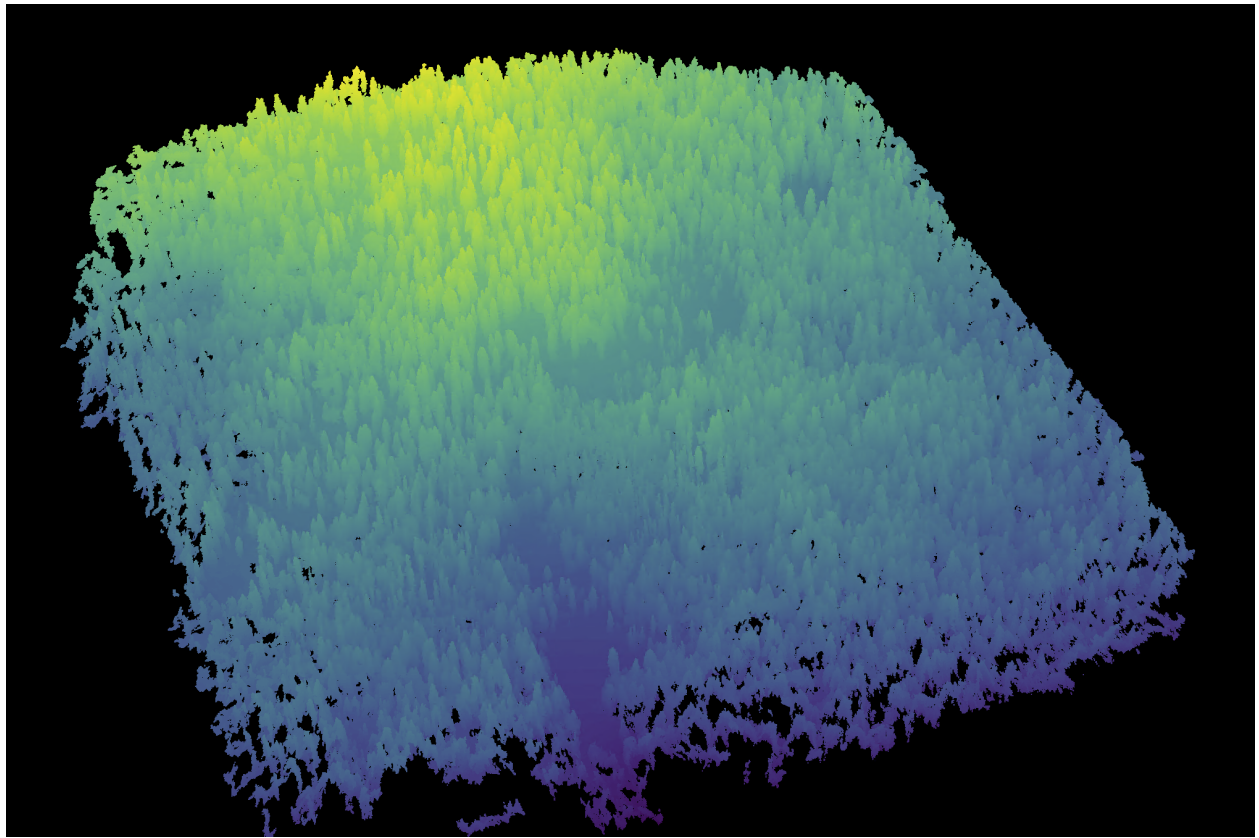


Figure 2: A dense point cloud representing ~40 hectares of forest is generated using Structure from Motion (SfM) processing of ~1900 images. The dense point cloud z- position represents the ground elevation plus the vegetation height.

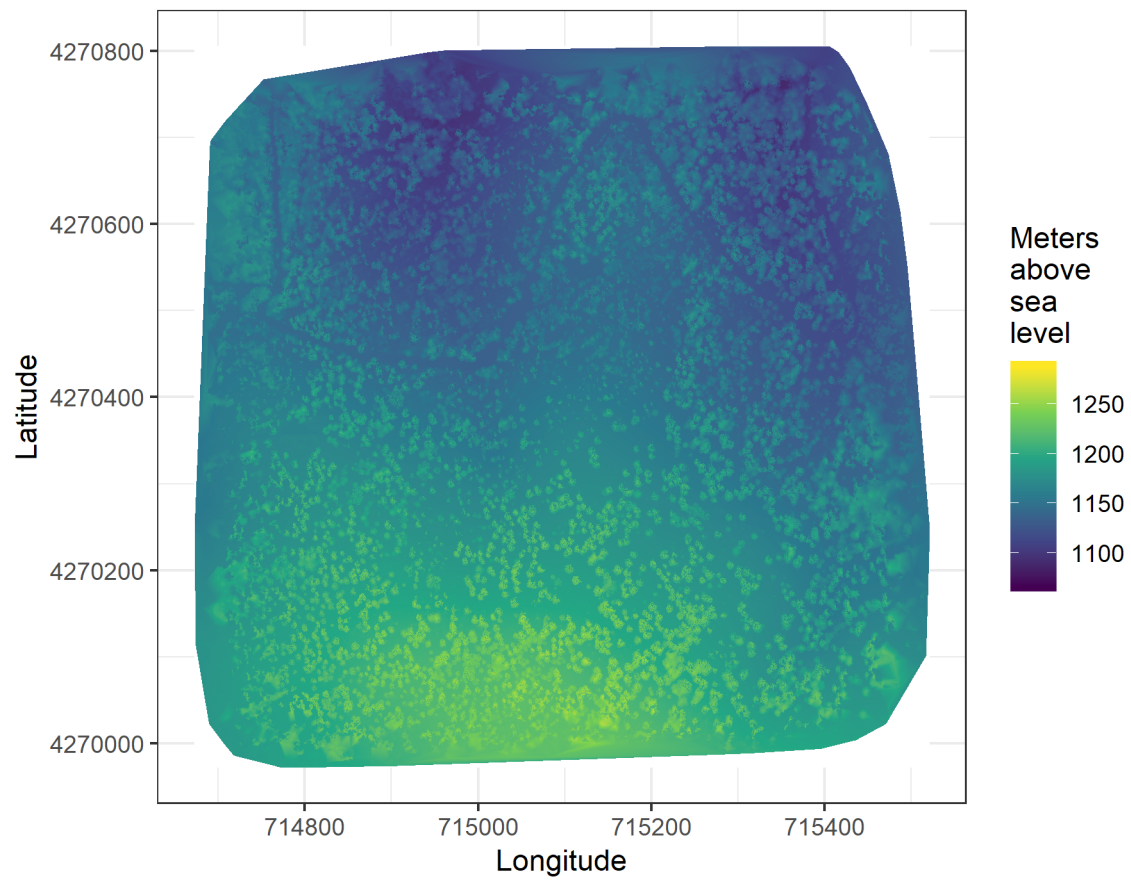


Figure 3: The digital surface model (DSM) is a 2-dimensional representation of the dense point cloud generated using structure from motion (SfM) processing. The DSM represents the ground elevation plus the vegetation height.

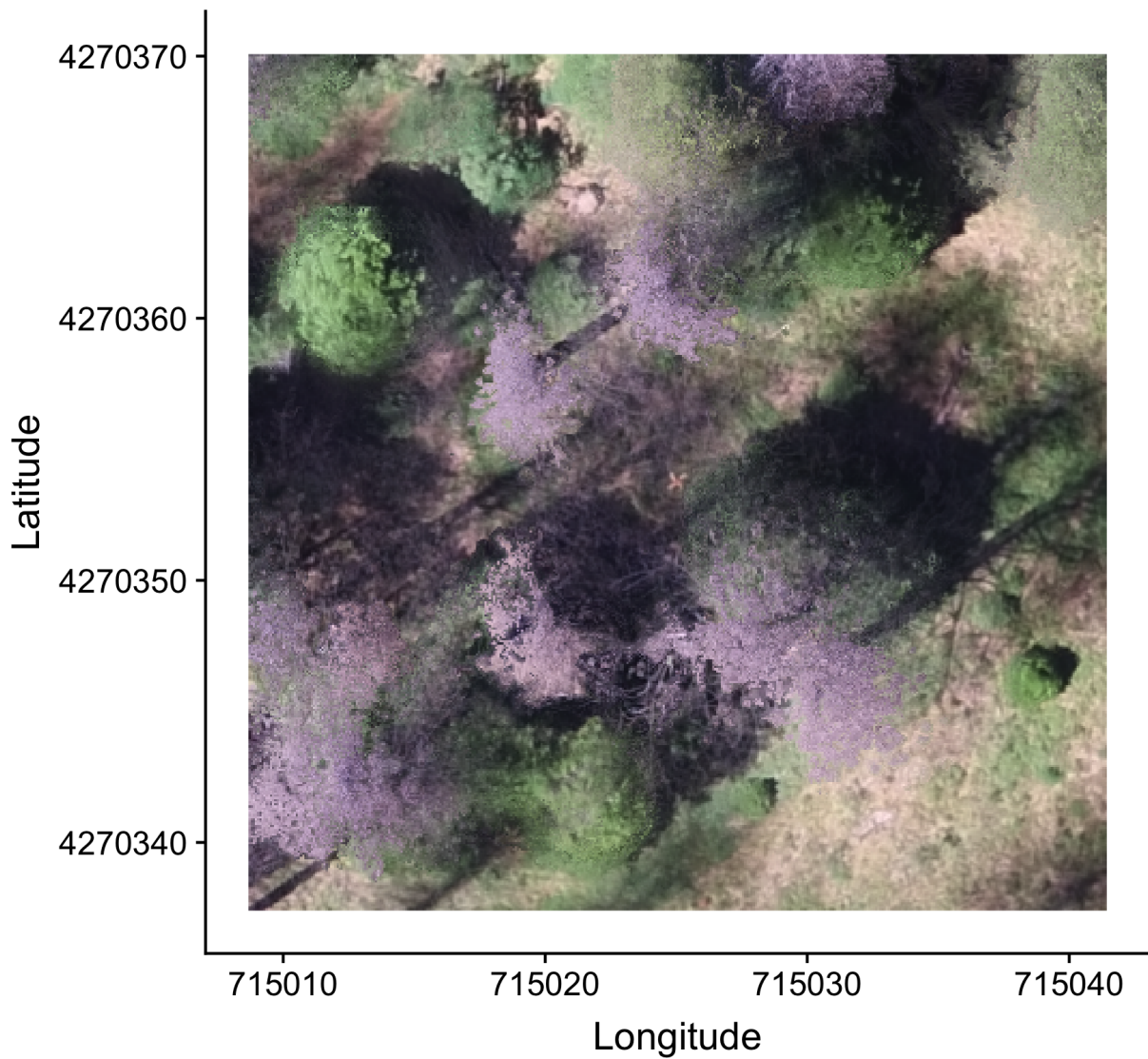


Figure 4: The orthomosaic for each of the 32 sites is generated with the Structure from Motion (SfM) processing, showing a top-down view of the whole survey area such that distances between objects in the scene are preserved and can be measured. Depicted is an example orthomosaic for one of the 32 sites cropped to the extent of a single ground plot (5 ground plots per site) showing the orange X placed at exactly the plot center prior to flight. The original orthomosaic for the whole site represents an area approximately 1000 times as large as the area depicted here.

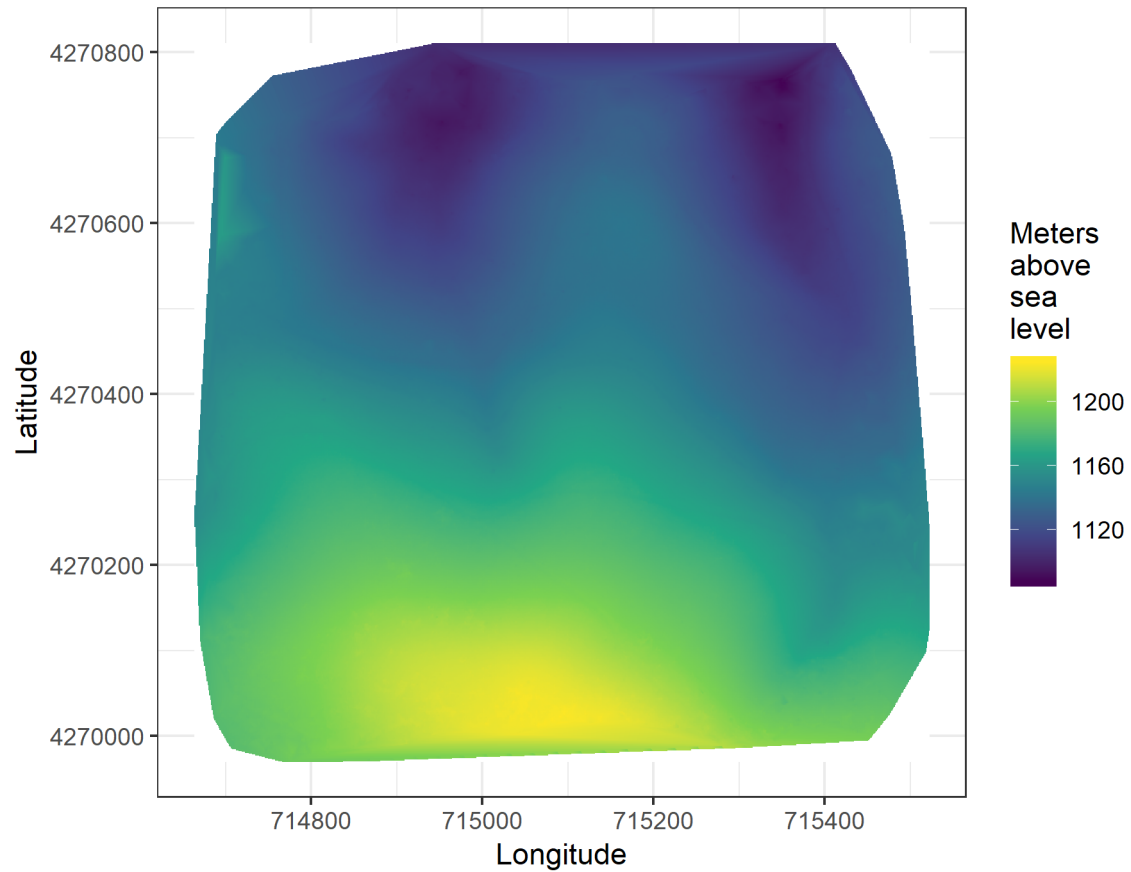


Figure 5: The digital terrain model (DTM) is generated by processing the dense point cloud using the cloth simulation filter algorithm (Zhang et al. 2016), which classifies points as ‘ground’ or ‘not-ground’ and then interpolates the ‘ground’ elevation using Delaunay triangulation for the rest of the dense point cloud footprint. The DTM represents the ground elevation without any vegetation.

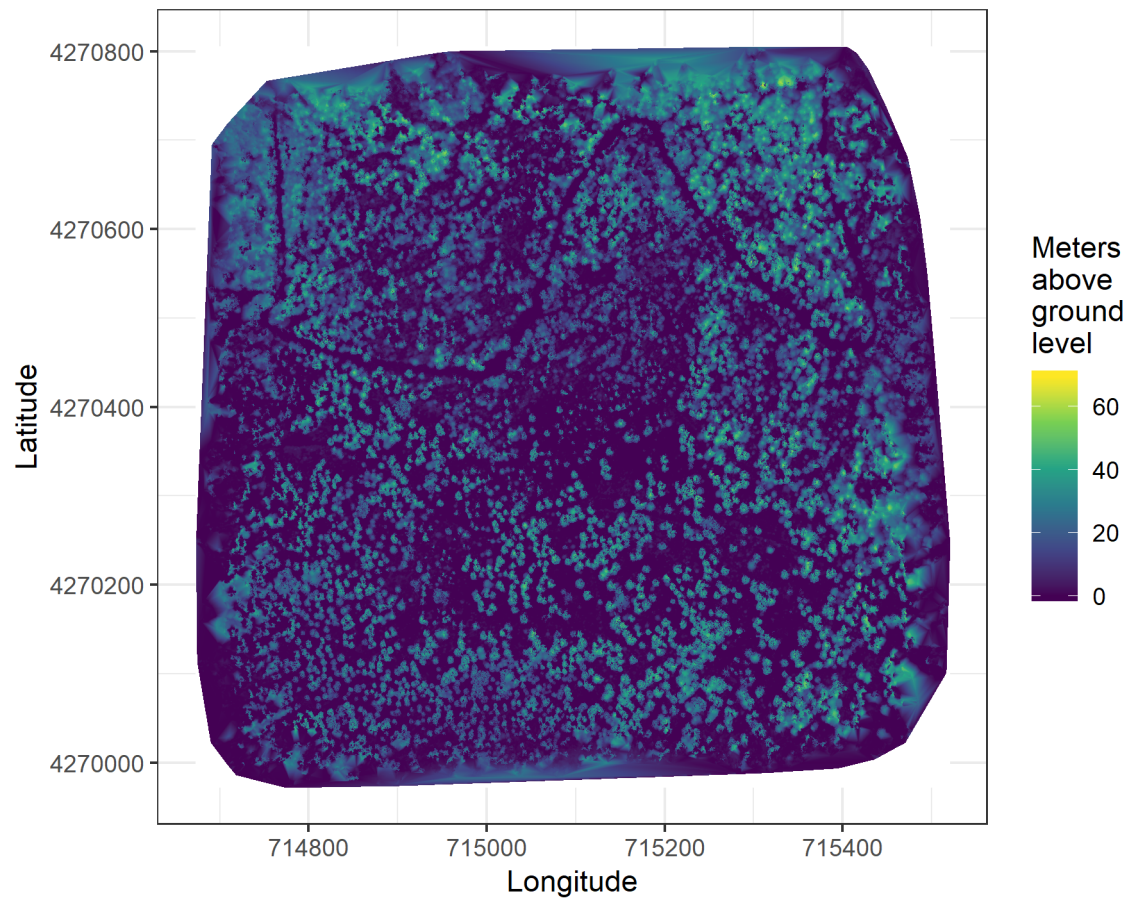


Figure 6: The canopy height model (CHM) is generated by subtracting the digital terrain model from the digital surface model. The CHM represents the height of all of the elevation above ground level.

205 the default `winFun` parameter for the `vwf()` function as well as the “pines” and “combined” functions from
 206 Popescu and Wynne (2004) as the `winFun` parameter. We used 6 parameter sets of a local maximum filter
 207 implemented in `lidR`. We used 131 parameter sets of the algorithm from Li et al. (2012), which operates on
 208 the original point cloud. These parameter sets included those from Shin et al. (2018) and Jakubowski et
 209 al. (2013). We used 3 parameter sets of the `watershed` algorithm implemented in `lidR`, which is a wrapper
 210 for a function in the `EBImage` package (Pau et al. 2010). We used 3 parameter sets of `ptrees` (Vega et al.
 211 2014) implemented in `lidR` (Roussel et al. 2019) and `lidRplugins` (Roussel 2019) and which operates on
 212 the raw point cloud, without first normalizing it to height above ground level (i.e.. subtracting the ground
 213 elevation from the dense point cloud). We used the default parameter set of the `multichm` (Eysn et al. 2015)
 214 algorithm implemented in `lidR` (Roussel et al. 2019) and `lidRplugins` (Roussel 2019). Finally, we used 30
 215 parameter sets of the experimental algorithm `lmfx` (Roussel 2019).

Table 2: Algorithm name, number of parameter sets tested for each algorithm, and references.

Algorithm	Parameter sets tested	Reference(s)
li2012	131	Li et al. (2012); Jakubowski et al. (2013); Shin et al. (2018)
lmfx	30	Roussel (2019)
localMaxima	6	Roussel et al. (2019)
multichm	1	Eysn et al. (2015)
ptrees	3	Vega et al. (2014)
vwf	3	Plowright (2018)
watershed	3	Pau et al. (2010)

216 Map ground data

217 Each orthorectified reflectance map was inspected to locate the 5 orange “X”s marking the center of the field
 218 plots (Figure 4), though some plot centers were obscured due to dense interlocking tree crowns or because a
 219 plot center was located directly under a single tree crown. We were able to locate 110 out of 180 field plots
 220 and were then able to use these plots for validation of automated tree detection algorithms. We used the `sf`
 221 package (Pebesma et al. 2019) to convert distance-from-center and azimuth measurements of each tree in the
 222 ground plots to an x-y position on the SfM-derived reflectance map using the x-y position of the orange X
 223 visible in the reflectance map as the center.

224 Correspondence of automatic tree detection with ground data

225 We calculated 7 forest structure metrics for each field plot using the ground data collected by Fettig et al.

226 (2019): total number of trees, number of trees greater than 15 meters, mean height of trees, 25th percentile

227 tree height, 75th percentile tree height, mean distance to nearest tree neighbor, mean distance to 2nd nearest

228 neighbor.

229 For each tree detection algorithm and parameter set described above, we calculated the same set of 7 structure

230 metrics within the footprint of the validation field plots. We calculated the Pearson's correlation and root

231 mean square error (RMSE) between the ground data and the aerial data for each of the 7 structure metrics

232 for each of the 177 automatic tree detection algorithms/parameter sets.

233 For each algorithm and parameter set, we calculated its performance relative to other algorithms as whether

234 its Pearson's correlation was within 5% of the highest Pearson's correlation as well as whether its RMSE

235 was within 5% of the lowest RMSE. For each algorithm/parameter set, we summed the number of forest

236 structure metrics for which it reached these 5% thresholds. For automatically detecting trees across the whole

237 study, we selected the algorithm/parameter set that performed well across the most number of forest metrics

238 (Figure 7).

239 Segmentation of crowns

240 We delineated individual tree crowns with a marker controlled watershed segmentation algorithm (Meyer and

241 Beucher 1990) using the detected treetops as markers implemented in the **ForestTools** package (Plowright

242 2018). If the automatic segmentation algorithm failed to generate a crown segment for a detected tree (e.g.,

243 often snags with a very small crown footprint), a circular crown was generated with a radius of 0.5 meters. If

244 the segmentation generated multiple polygons for a single detected tree, only the polygon containing the

245 detected tree was retained (Figure 8). Image overlap decreases near the edges of the overall flight path, which

246 reduces the quality of the SfM processing in those areas. Thus, we excluded segmented crowns within 35

247 meters of the edge of the survey area. Given the narrower field of view of the RedEdge3 multispectral camera

248 versus the X3 RGB camera whose optical parameters were used to define the ~40 hectare survey area around

249 each site, as well as the 35 meter additional buffering, the survey area at each site was approximately 30

250 hectares (Table 3).

251 We used the **velox** package (Hunziker 2017) to extract all the pixel values from the orthorectified reflectance

252 map for each of the 5 narrow bands within each segmented crown polygon. Per pixel, we additionally

253 calculated the normalized difference vegetation index (NDVI; Rouse et al. (1973)), the normalized difference

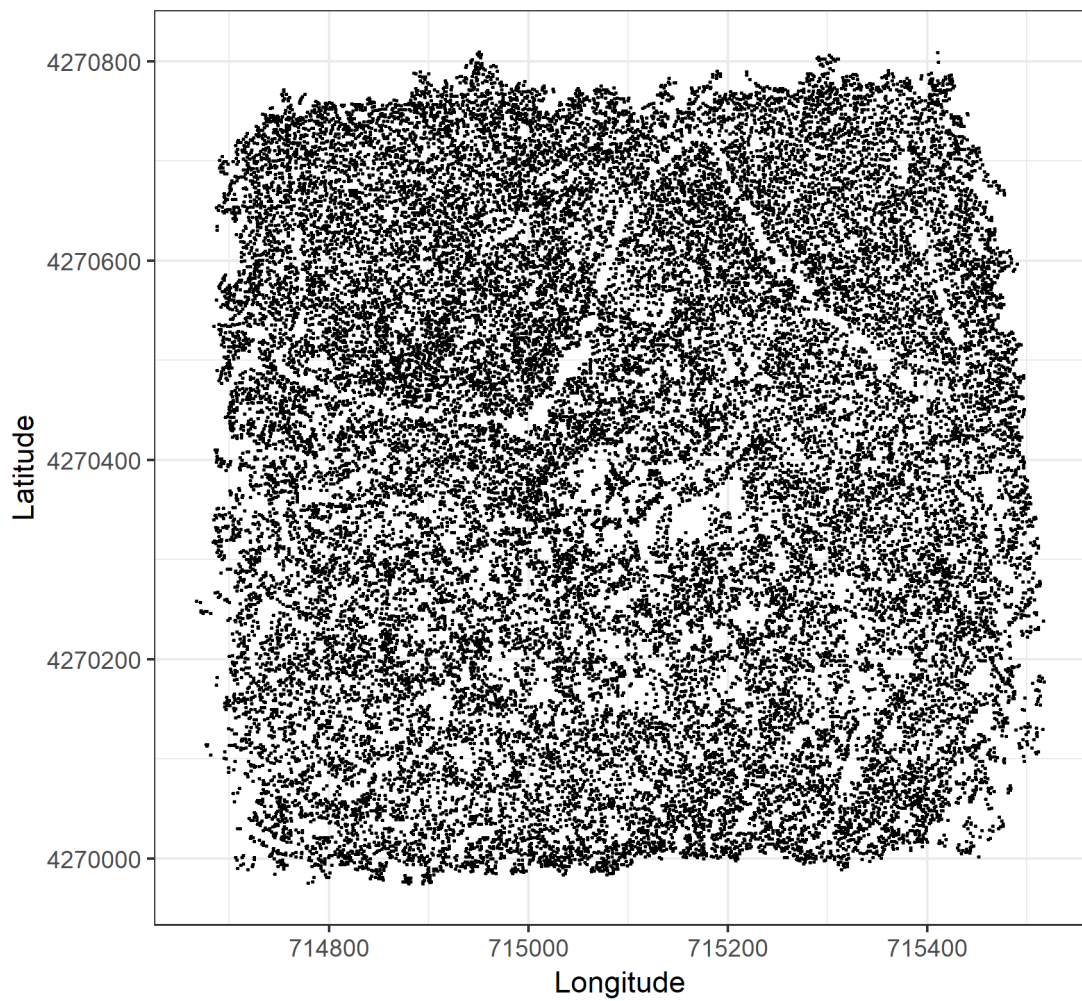


Figure 7: Tree locations are detected using the `lmfx` (Roussel et al. 2019) treetop detection algorithm on the dense point cloud.

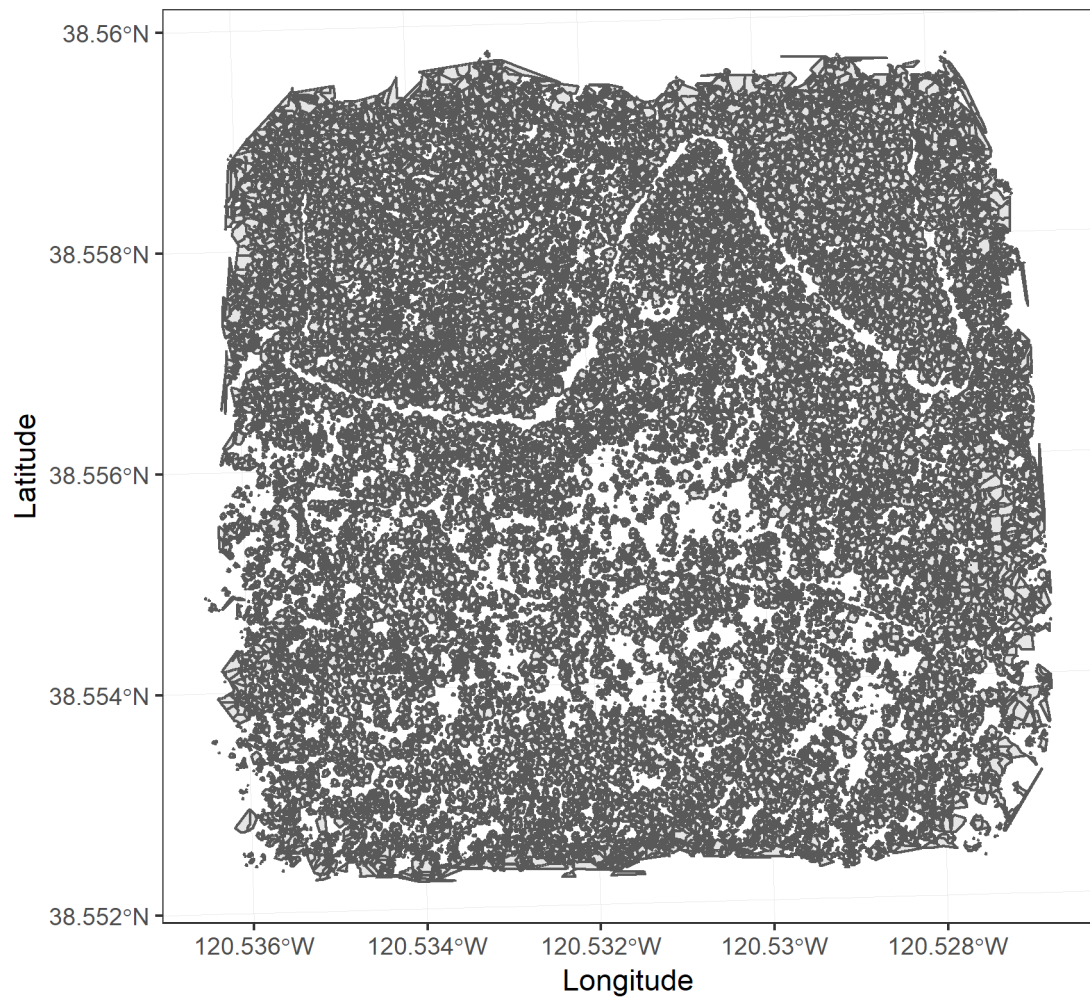


Figure 8: Individual crowns are delineated using a marker controlled watershed segmentation algorithm (Meyer and Beucher 1990, Plowright 2018) on the canopy height model (CHM) using the detected tree locations as a priority map. If the algorithm failed to delineate a crown for a tree that was identified in the tree detection step, a circular crown with a 0.5m buffer centered on point location of the detected tree was added as a crown.

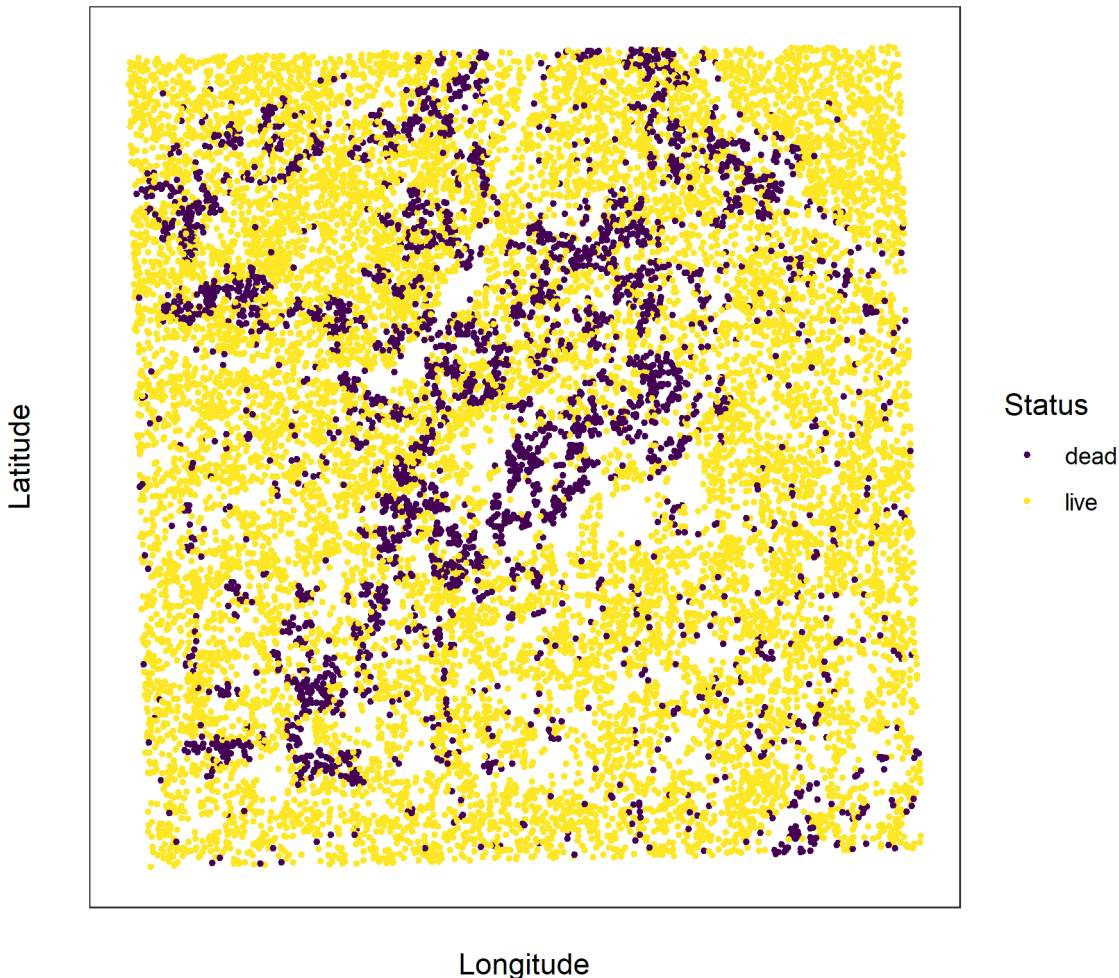


Figure 9: Each tree is classified as live or dead by extracting the pixel values from the 5 narrow bands of the Rededge3 camera (and 5 derived bands— see methods) in the orthomosaic within each segmented tree crown of the detected trees, taking their mean value, and using those means to predict live/dead status with a boosted logistic regression previously trained on a hand-classified set of segmented crowns from across the study area.

254 red edge (NDRE; Gitelson and Merzlyak (1994)), the red-green index (RGI; Coops et al. (2006)), the red
 255 edge chlorophyll index ($CI_{red\ edge}$; Clevers and Gitelson (2013)), and the green chlorophyll index (CI_{green} ;
 256 Clevers and Gitelson (2013)). For each crown polygon, we calculated the mean value for each raw and derived
 257 reflectance band (5 raw; 5 derived).

258 **Classification of trees**

259 We overlaid the segmented crowns on the reflectance maps from 20 sites spanning the latitudinal and elevation
 260 gradient in the study. Using QGIS, we hand classified 564 trees as live/dead (Figure 9) and as one of 5
 261 dominant species in the study area (*Pinus ponderosa*, *Pinus lambertiana*, *Abies concolor*, *Calocedrus decurrens*,

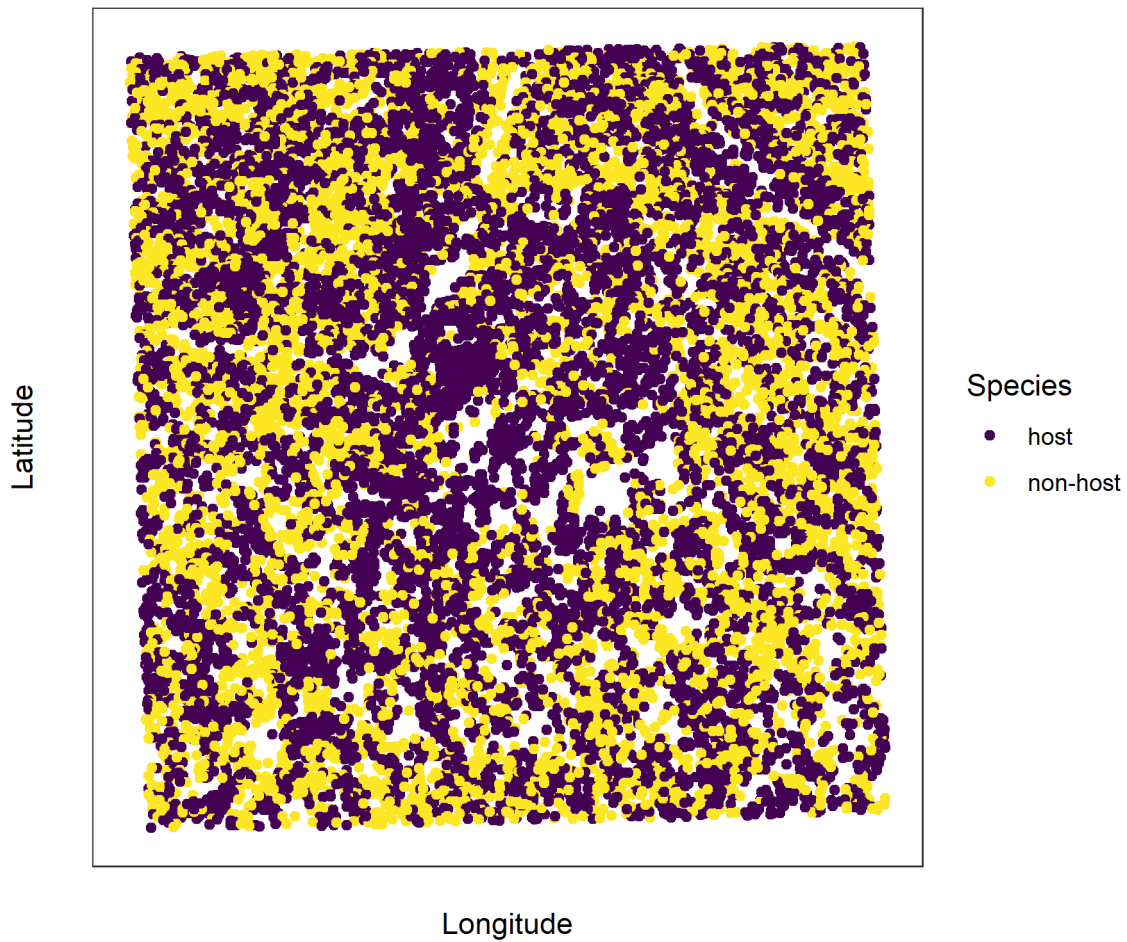


Figure 10: For each live tree, we classified its species using the same means of extracted pixel values across the 5 Rededge3 narrow bands (and 5 derived bands) as predictors in a regularized discriminant analysis previously trained on a hand-classified set of segmented crowns from across the study area.

262 or *Quercus kelloggii*) using the mapped ground data as a guide. We treated all trees classified as ponderosa
263 pine as a “host” tree and all other species as “non-host” trees (Figure 10).

264 We used all 10 mean values of the reflectance bands for each tree crown polygon to predict whether the hand
265 classified trees were alive or dead using a boosted logistic regression model implemented in the **caret** package
266 (accuracy of live/dead classification on a withheld test dataset: 97.3%) (Kuhn 2008). For just the living trees,
267 we similarly used all 10 reflectance values to predict the tree species using regularized discriminant analysis
268 implemented in the **caret** package (accuracy of species classification on a withheld testing dataset: 66.7%;
269 accuracy of WPB host/non-WPB-host (i.e., ponderosa pine versus other tree species) on a withheld testing
270 dataset: 74.4%).

271 Finally, we used these models to classify all tree crowns in the data set as alive or dead as well as the species
272 of living trees.

273 **Allometric scaling of height to quadratic mean diameter**

274 We converted the height of each tree determined using the canopy height model to its diameter at breast
275 height, 1.37m (DBH). Using the tree height and DBH ground data from Fettig et al. (2019), we fit a simple
276 linear regression to predict DBH from height for each of the 5 dominant species. Using the model-classified
277 tree species of each segmented tree, we used the corresponding linear relationship for that species to estimate
278 the DBH given the tree’s height. We then calculated the quadratic mean diameter for each 20m x 20m cell as
279 the square root of the average squared diameter of trees within the cell.

280 **Note on assumptions about dead trees**

281 For the purposes of this study, we assumed that all dead trees were ponderosa pine and were thus host trees
282 for the western pine beetle. This is a reasonably good assumption for our study area, given that Fettig et al.
283 (2019) found that 73.4% of the dead trees in the coincident ground plots were ponderosa pine. The species
284 contributing to the next highest proportion of dead trees was incense cedar which represented 18.72% of the
285 dead trees in the ground plots. Incense cedar is not a potential host of the western pine beetle, and different
286 forest structure/environment conditions can dictate the dynamic between forest insects and their host tree
287 species (Stephenson et al. 2019). While the detected mortality is most likely to be ponderosa pine, it is
288 critical to interpret our results with this known limitation in mind.

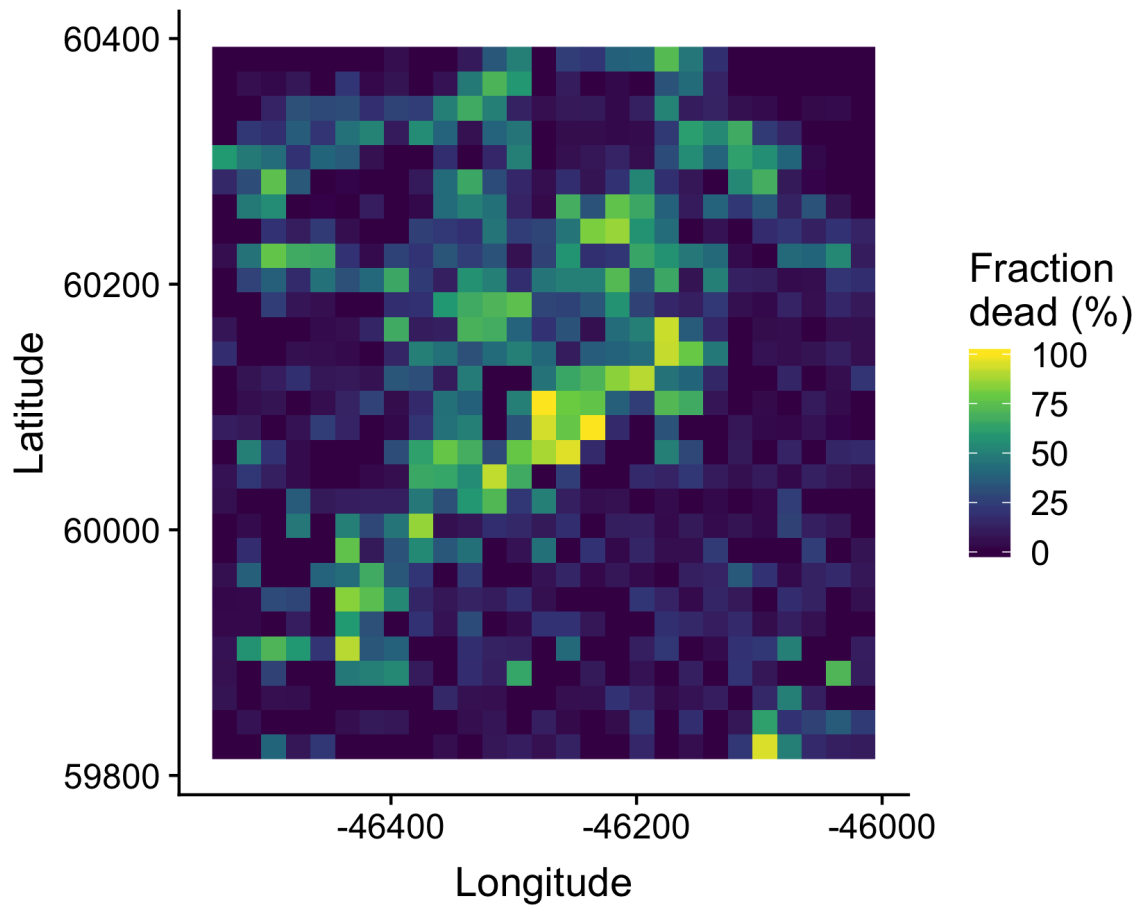


Figure 11: We rasterized the individual tree data by aggregating values to 20m x 20m cells. This example shows the proportion of dead trees per cell for the same example site as in the previous figures.

289 **Rasterizing individual tree data**

290 Because the tree detection algorithms were validated against ground data at the plot level, we rasterized the
291 classified trees at a spatial resolution similar to that of the ground plots (Figure 11). That is, we rasterized
292 the individual tree data to 20m x 20m pixels equaling 400 m², and the circular ground plots with 11.35m
293 radius covered 404 m². In each raster cell, we calculated the: number of live trees, number of dead trees,
294 number of ponderosa pine trees, total number of trees (of all species, including ponderosa pine), quadratic
295 mean diameter (QMD) of ponderosa pine trees, and QMD of all trees of any species (overall QMD). We
296 converted the count of ponderosa pine trees and the total tree count to a density measurement of trees per
297 hectare (tpha) by multiplying the counts in each 20m x 20m cell by 25 to create a “host density” and an
298 “overall density” variable per cell.

299 **Environmental data**

300 We used climatic water deficit (CWD) (Stephenson 1998) from the 1981-2010 mean value of the basin
301 characterization model (Flint et al. 2013) as an integrated measure of temperature and moisture conditions
302 for each of the 32 sites. Higher values of CWD correspond to hotter, drier conditions and lower values
303 correspond to cooler, wetter conditions. CWD has been shown to correlate well with broad patterns of tree
304 mortality in the Sierra Nevada (Young et al. 2017) as well as bark beetle-induced tree mortality (Millar et al.
305 2012). We converted the CWD value for each site into a z-score representing that site’s deviation from the
306 mean CWD across the climatic range of Sierra Nevada ponderosa pine as determined from 179 herbarium
307 records described in Baldwin et al. (2017). Thus, a CWD z-score of one would indicate that the CWD at
308 that site is one standard deviation hotter/drier than the mean CWD across all geolocated herbarium records
309 for ponderosa pine in the Sierra Nevada.

310 **Statistical model**

311 We used a generalized linear model with a zero-inflated binomial response and a logit link to predict the
312 probability of ponderosa pine mortality within each 20m x 20m cell as a function of the crossed effects of
313 ponderosa pine quadratic mean diameter and density added to the crossed effect of quadratic mean diameter
314 and density of trees of all species in each cell (hereafter “overall quadratic mean diameter” and “overall
315 density”), as well as the interaction of each summand with climatic water deficit at each site.

316 To measure and account for spatial autocorrelation of the bark beetle behavioral processes underlying
317 ponderosa pine mortality, we subsampled the data at each site to a random selection of 200, 20m x 20m cells
318 representing approximately 27.5% of the surveyed area. With these subsampled data, we included a separate

319 exact Gaussian process term per site of the interaction between the x- and y-position of each cell using the
 320 `gp()` function in the `brms` package (Bürkner 2017). The Gaussian process estimates the spatial covariance in
 321 the response variable (log-odds of ponderosa pine mortality) jointly with the effects of the other covariates.

$$y_{i,j} \sim \begin{cases} 0, & p \\ Binom(n_i, \pi_i), & 1 - p \end{cases}$$

$$\begin{aligned} logit(\pi_i) = & \beta_0 + \\ & \beta_1 X_{cwd,j} + \\ & \beta_1 X_{cwd,j} (\beta_2 X_{\text{pip}oQMD,i} + \beta_3 X_{\text{pip}oDensity,i} + \beta_4 X_{\text{pip}oQMD,i} X_{\text{pip}oDensity,i}) + \\ & \beta_1 X_{cwd,j} (\beta_5 X_{\text{overall}QMD,i} + \beta_6 X_{\text{overall}Density,i} + \beta_7 X_{\text{overall}QMD,i} X_{\text{overall}Density,i}) + \\ & \mathcal{GP}_j(x_i, y_i) \end{aligned}$$

322 Where y_i is the number of dead trees in cell i , n_i is the sum of the dead trees (assumed to be ponderosa pine)
 323 and live ponderosa pine trees in cell i , π_i is the probability of ponderosa pine tree mortality in cell i , p is the
 324 probability of there being zero dead trees in a cell arising as a result of an unmodeled process, $X_{cwd,j}$ is the
 325 z-score of climatic water deficit for site j , $X_{\text{pip}oQMD,i}$ is the scaled quadratic mean diameter of ponderosa
 326 pine in cell i , $X_{\text{pip}oDensity,i}$ is the scaled density of ponderosa pine trees in cell i , $X_{\text{overall}QMD,i}$ is the scaled
 327 quadratic mean diameter of all trees in cell i , $X_{\text{overall}Density,i}$ is the scaled density of all trees in cell i , x_i
 328 and y_i are the x- and y- coordinates of the centroid of the cell in an EPSG3310 coordinate reference system,
 329 and \mathcal{GP}_j represents the exact Gaussian process describing the spatial covariance between cells at site j .

330 We used 4 chains with 2000 iterations each (1000 warmup, 1000 samples), and confirmed chain convergence
 331 by ensuring all `Rhat` values were less than 1.1 (Brooks and Gelman 1998). We used posterior predictive
 332 checks to visually confirm model performance by overlaying the density curves of the predicted number of
 333 dead trees per cell over the observed number (Gabry et al. 2019). For the posterior predictive checks, we
 334 used 50 random samples from the model fit to generate 50 density curves and ensured curves were centered
 335 on the observed distribution, paying special attention to model performance at capturing counts of zero.

336 Software and data availability

337 All data are available via the Open Science Framework. Statistical analyses were performed using the `brms`
 338 packages. With the exception of the SfM software (Pix4Dmapper Cloud) and the GIS software QGIS, all
 339 data carpentry and analyses were performed using R (R Core Team 2018).

³⁴⁰ **Results**

Table 3: Site characteristics for each of the 32 sites. The site name consists of the forest name, elevation band, and rep separated by an underscore. The Eldorado National Forest is ‘eldo’, the Stanislaus National Forest is ‘stan’, the Sierra National Forest is ‘sier’, and the Sequoia National Forest is ‘sequ’. The elevation band represents the lower bounds of the 305 meter (1000 foot) elevation bands in feet. Thus ‘3k’ implies that site was located between 3,000 and 4,000 feet (914-1219 meters). Aerially detected mortality and density of the whole site is presented along with the mortality and density calculated from the ground data (aerial / ground). The density is measured in trees per hectare (tpha).

Site	CWD (mm)	CWD (z-score)	Survey area (ha)	% tree mortality (aerial/ground)	Density (tpha; aerial/ground)
eldo_3k_1	678	0.319	31.02	11/61	630/410
eldo_3k_2	706	0.501	30.61	12/36	444/647
eldo_3k_3	655	0.163	30.95	22/36	493/410
eldo_4k_1	570	-0.383	28.04	9/39	633/588
eldo_4k_2	642	0.0831	28.41	15/78	338/272
eldo_5k_1	663	0.219	28.44	11/44	662/544
eldo_5k_2	627	-0.0132	30.02	12/36	585/969
eldo_5k_3	599	-0.2	29.73	7/32	489/623
stan_3k_1	638	0.059	31.04	10/52	739/1038
stan_3k_2	739	0.713	18.78	40/78	434/405
stan_3k_3	762	0.859	30.1	22/41	558/326
stan_4k_1	540	-0.58	29.62	29/63	508/712
stan_4k_2	528	-0.658	30.54	18/56	482/257
stan_5k_1	524	-0.688	30.94	19/54	389/336
stan_5k_2	524	-0.685	29.94	21/44	399/623
sier_3k_1	764	0.871	30.42	19/48	651/850
sier_3k_2	768	0.898	30.05	20/77	439/153
sier_3k_3	773	0.932	29.77	32/77	511/460
sier_4k_1	841	1.38	30.43	54/51	576/539
sier_4k_2	764	0.877	29.3	33/57	499/855
sier_4k_3	688	0.383	26.39	48/59	454/499
sier_5k_1	722	0.599	14.59	41/43	631/717
sier_5k_2	710	0.523	27.53	53/74	477/455
sier_5k_3	779	0.968	28.93	33/43	569/484

Site	CWD (mm)	CWD (z-score)	Survey area (ha)	% tree mortality (aerial/ground)	Density (tpha; aerial/ground)
sequ_4k_1	767	0.891	29.59	50/56	366/608
sequ_4k_3	816	1.21	29.69	35/71	433/306
sequ_5k_1	718	0.577	27.12	35/52	364/445
sequ_5k_2	587	-0.274	29.1	45/43	478/499
sequ_5k_3	611	-0.117	31.34	42/48	349/494
sequ_6k_1	731	0.657	27.78	30/70	433/361
sequ_6k_2	690	0.39	11.83	26/43	699/934
sequ_6k_3	603	-0.174	26.51	36/32	536/692

341 Tree detection

342 We found that the experimental `lmfx` algorithm with parameter values of `dist2d = 1` and `ws = 2.5` (Roussel
 343 et al. 2019) performed the best across 7 measures of forest structure as measured by Pearson’s correlation
 344 with ground data (Table 4).

Table 4: Correlation and differences between the best performing tree detection algorithm (`lmfx` with `dist2d = 1` and `ws = 2.5`) and the ground data. An asterisk next to the correlation or RMSE indicates that this value was within 5% of the value of the best-performing algorithm/parameter set. Ground mean represents the mean value of the forest metric across the 110 ground plots that were visible from the sUAS-derived imagery. The median error is calculated as the median of the differences between the air and ground values for the 110 visible plots. Thus, a positive number indicates an overestimate by the sUAS workflow and a negative number indicates an underestimate.

Forest structure metric	Ground mean	Correlation with ground	RMSE	Median error
total tree count	19	0.67*	8.68*	2
count of trees > 15m	9.9	0.43	7.38	0
distance to 1st neighbor (m)	2.8	0.55*	1.16*	0.26
distance to 2nd neighbor (m)	4.3	0.61*	1.70*	0.12
height (m); 25th percentile	12	0.16	8.46	-1.2
height (m); mean	18	0.29	7.81*	-2.3
height (m); 75th percentile	25	0.35	10.33*	-4

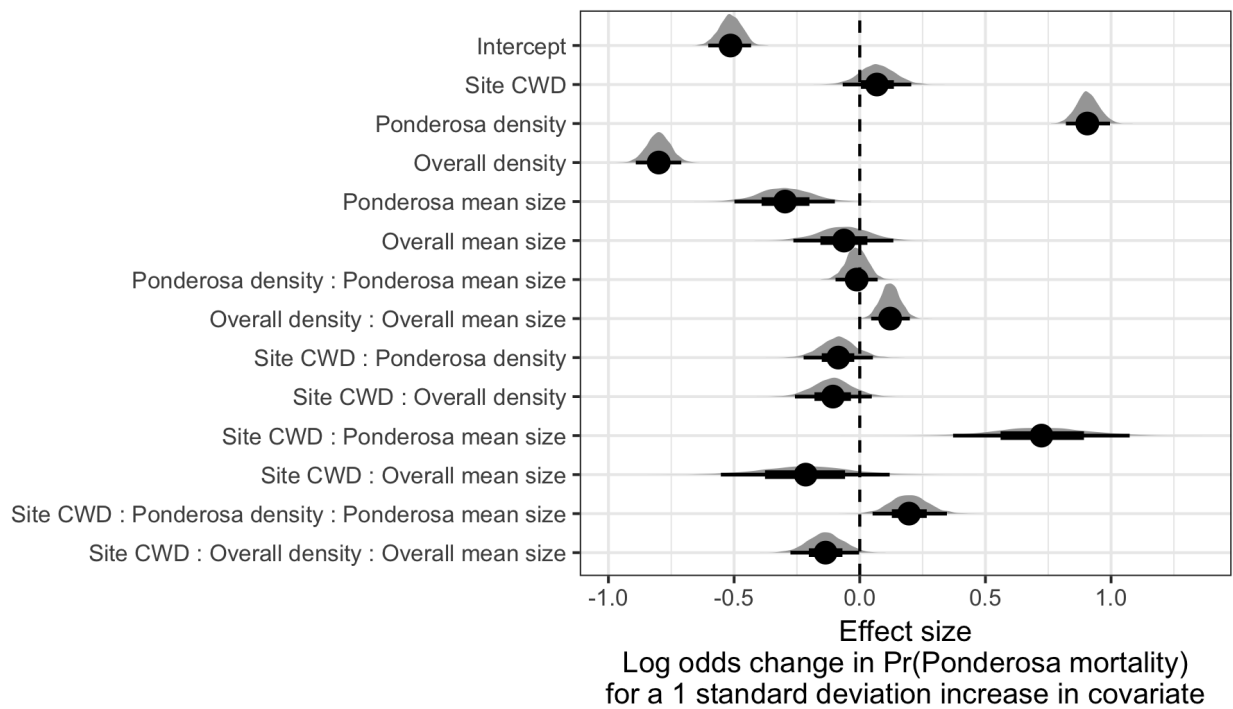


Figure 12: Posterior distributions of effect size from zero-inflated binomial model predicting the probability of ponderosa pine mortality in a 20m x 20m cell given forest structure characteristics of host trees and all trees within the cell, as well as a site-level climatic water deficit. The gray density distribution for each model covariate represents the density of the posterior distribution, the point underneath each density curve represents the median of the estimate, the bold interval surrounding the point estimate represents the 66% credible interval, and the thin interval surrounding the point estimate represents the 95% credible interval.

345 Effect of local structure and regional climate on western pine beetle severity

346 We detected a small, generally positive main effect of climatic water deficit on the probability of ponderosa
347 pine mortality within each 20m x 20m cell (Figure 12).

348 We found a strongly positive main effect of ponderosa pine local density, with greater density increasing the
349 probability of ponderosa pine mortality. Conversely, we found a strong negative effect of overall tree density
350 (i.e., including both ponderosa pine and non-host species) such that additional non-host trees in a 20m x 20m
351 cell (for the same number of host trees) would decrease the probability of ponderosa pine mortality (Figure
352 12).

353 We found a generally negative effect of quadratic mean diameter of ponderosa pine on the probability of
354 ponderosa mortality, suggesting that the western pine beetle attacked smaller trees, on average. There was a
355 strong positive interaction between the climatic water deficit and ponderosa pine quadratic mean diameter,
356 such that larger trees were more likely to increase the probability of ponderosa mortality in hotter, drier sites
357 (Figure 13).

358 There was a positive interaction between overall tree density and overall quadratic mean diameter, such that
359 denser stands with larger trees did lead to greater ponderosa pine mortality, though the main effects of each
360 of these variables were weakly negative (Figure 12).

361 Discussion

362 We found that host tree density is a dominant driver of host mortality during elevated levels of bark beetle
363 activity, likely due to energy costs associated with beetles navigating forests with many non-hosts available.

364 We also found that, even within a single forest insect/tree species pairing, in the same extreme drought,
365 and conditional upon high levels of western pine beetle activity, host tree size may still strongly affect
366 insect-induced tree mortality in different ways depending on background environmental conditions of water
367 stress. We suggest that this may indicate different stages of bark beetle disturbance throughout the Sierra
368 yellow pine/mixed-conifer system, with “outbreak” thresholds surpassed at the hottest, driest sites where
369 larger trees led to more likely host mortality, but not yet surpassed in cooler, wetter sites, where smaller trees
370 led to more likely host mortality.

371 Broad-scale environmental condition

372 We were surprised to only find a weakly positive main effect of climatic water deficit on the probability of
373 ponderosa mortality, though an effect did materialize through its interaction with forest structure. We did

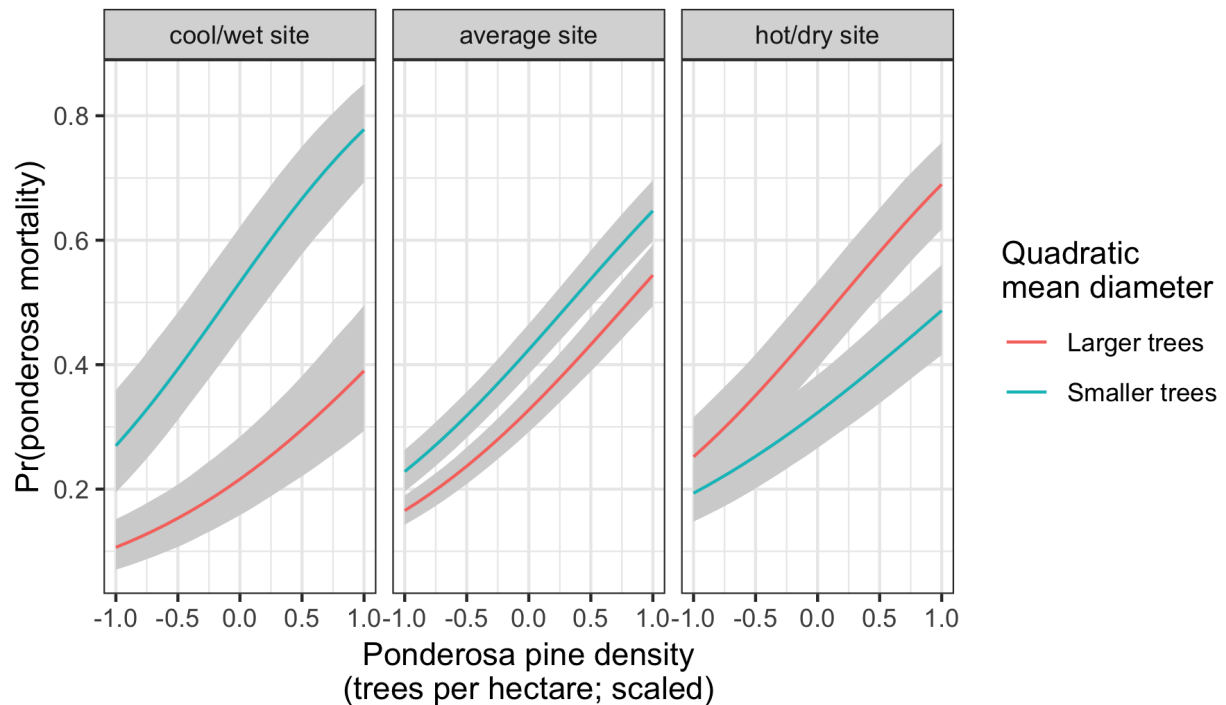


Figure 13: Line version of model results with 95% credible intervals showing primary influence of ponderosa pine structure on the probability of ponderosa pine mortality, and the interaction across climatic water deficit. The 'larger trees' line represents the quadratic mean diameter of ponderosa pine 0.7 standard deviations above the mean, and the 'smaller trees' line represents the quadratic mean diameter of ponderosa pine 0.7 standard deviations below the mean.

374 not measure tree water stress at an individual tree level as in other recent work (Stephenson et al. 2019), and
375 were instead treating climatic water deficit as a general indicator of tree stress following results of coarser-scale
376 studies (Asner et al. 2016, Young et al. 2017) which may have contributed to our failure to detect a strong
377 effect. Also, our entire study area experienced the same extreme hot drought between 2012 and 2015 and the
378 variation of mortality explained by a main effect of climatic water deficit may be dampened when most trees
379 are experiencing a high degree of water stress (Floyd et al. 2009, Fettig et al. 2019).

380 **Strength of support for different “density increases mortality” hypotheses**

381 The strongest effect on the probability of host mortality was the local host density within each 20m x 20m
382 cell. Host availability has been shown to have a strong influence on the prevalence of host mortality (Raffa
383 and Berryman 1987). This can arise as beetles require shorter flights to disperse to new hosts and beetles are
384 less likely to land on a non-host tree which imposes a “sunk cost” of energy expenditure in getting to that
385 tree. Reduced dispersal distances to host trees likely favors successful bark beetle attacks, but we calibrated
386 our aerial tree detection to ~400 m² areas rather than to individual tree locations so don’t have the data
387 precision to address this hypothesis directly. Because we also found a strong negative effect of overall tree
388 density (host plus non-host) within each cell while accounting for host density, we suspect that the positive
389 association between host density and host mortality might be driven by increasing the frequency that western
390 pine beetles land on their preferred host and avoid expending energy flying to non-hosts. The negative
391 relationship that we detected between overall tree density and host mortality corroborates findings from
392 Fettig et al. (2019) and perhaps the “sunk cost” of landing on non-hosts explains those findings, though
393 Fettig et al. (2019) didn’t simultaneously model the effect of host density. In general, Hayes et al. (2009)
394 and Fettig et al. (2019) found that measures of host availability explained less variation in mortality than
395 measures of overall tree density, but those conclusions were based on a response variable of “total number of
396 dead host trees,” rather than the number of dead host trees conditional on the total number of host trees as
397 in our study (i.e., a binomial response).

398 Counter to our expectations, we found an overall negative effect of host tree mean size on the probability of
399 host mortality. Generally, smaller trees are easier for western pine beetles to overwhelm in a mass attack and
400 are prime targets under normal levels of tree water stress. However, larger trees are more nutritious and
401 are therefore ideal targets if local bark beetle density is high enough to successfully initiate mass attack as
402 can occur when many trees are under severe water stress (Bentz et al. 2010). In the recent hot drought, we
403 expected that most trees would be under severe water stress, setting the stage for increasing beetle density,
404 successful mass attacks, and targeting of larger trees. Larger average tree size in this case would therefore

405 lead to greater ponderosa pine mortality, as was found in coincident ground plots (Fettig et al. 2019) and
406 other studies (Stephenson et al. 2019, Pile et al. 2019). One possible explanation for our finding is that our
407 observations represent the cumulative mortality of trees during a multi-year drought event and its aftermath.
408 Lower host tree mean size led to a greater probability of host mortality earlier in the drought (Pile et al.
409 2019) and that signal might have persisted even as mortality continued to accumulate driven by other factors.

410 We did find a clear host tree size effect in its interaction with the climatic water deficit. In hot, dry sites,
411 larger average host size increased the probability of host mortality while smaller host sizes increased the
412 probability of host mortality in cool, wet sites. This suggests that the same bark beetle species was cueing
413 into different aspects of forest structure across the environmental gradient. This represents an intraspecific
414 version of the results of Stephenson et al. (2019), who found that insect-induced tree mortality in the same
415 region during the same hot drought were driven by different factors for different tree species. For instance,
416 Stephenson et al. (2019) found that ponderosa pine mortality was largely driven by host selection behavior
417 of forest insects, where larger more nutritious trees were specifically targeted regardless of whether they
418 exhibited signs of stress. In contrast, Stephenson et al. (2019) found that white fir mortality occurred
419 predominantly in the slower growing, smaller, stressed trees. In our study, we found that, even within a single
420 pairing of forest insect species and its host, the host tree size affected host mortality differently depending on
421 the site-level climatic water deficit.

422 For aggressive bark beetles, massive tree mortality as observed from the 2012-2015 drought and its aftermath
423 does not necessarily distinguish “endemic” from “outbreak” phases of bark beetle disturbance, which is
424 instead distinguished by the underlying driver of bark beetle host selection behavior (Logan et al. 1998).
425 “Endemic” phases are distinguished by environmental determinism, when beetles select hosts based on whether
426 they are weakened in some way, often by environmental conditions. “Outbreak” phases are distinguished
427 by dynamic determinism, when population dynamics reign—when local beetle density is high enough that
428 intraspecific pheromone communication dominates host selection, successful mass attacks are likely, and even
429 large healthy trees can be killed (White and Powell 1997, Logan et al. 1998). Despite high local levels of
430 tree mortality across our study area (Fettig et al. 2019), our results from surveying the broader context
431 surrounding coincident ground plots reveals different effects of host tree size depending on the climatic water
432 deficit, and perhaps different stages of bark beetle disturbance across the environmental gradient. This may
433 help explain the especially high host mortality in high host density, low host size cells that we observed
434 in cool/wet sites (Figure 13). The smaller trees would presumably be nutritionally sub-optimal, and thus
435 unexpected targets if the western pine beetle were indeed in an “outbreak” phase at these sites and able to
436 attack even large, healthy trees. While trees were likely water stressed across the whole study due to the

437 extreme drought, we expected generally less water stress in the cool/wet sites, and generally higher water
438 stress in the hot/dry sites (Asner et al. 2016, Young et al. 2017). Thus, it is possible that the observed
439 mortality patterns across the Sierra Nevada during the 2012-2015 hot drought arose as synergistic alignment
440 of environmental conditions and complex forest structure enabled the western pine beetle to cross thresholds
441 of “outbreak” behavior in the hottest, driest sites but such an alignment was not present in the cooler, wetter
442 sites (Raffa et al. 2008).

443 **Limitations and future directions**

444 We have demonstrated that drones can be effective means of collecting data at multiple, vastly different
445 spatial scales to investigate a single, multi-scale phenomenon– from meters in between trees, to hundreds of
446 meters of elevation, to hundreds of thousands of meters of latitude. However, some limitations remain but
447 could perhaps be overcome with further refinements in the use of this tool for forest ecology. Most of these
448 limitations arise from tree detection and classification uncertainty, and thus it was imperative to work with
449 field data for calibration and uncertainty reporting.

450 The greatest limitation in our study arising from classification uncertainty is in the assumption that all dead
451 trees were ponderosa pine. We estimate from coincident ground plots that this is true approximately 73.4%
452 of the time. Because tree mortality response to forest insects is species-specific, even with sympatric tree
453 species during the same hot drought (Stephenson et al. 2019), we cannot entirely rule out that some of the
454 mortality responses to complex forest structure that we observed arose from these species-specific responses.
455 The overall community composition across our study area was not very different (Fettig et al. 2019), so we
456 remain confident that the patterns we observed were driven primarily by the dynamic between the western
457 pine beetle and ponderosa pine.

458 Our ability to detect trees using the geometry of the dense point clouds derived with the SfM was also
459 limited. The horizontal accuracy of the tree detection was better than the vertical accuracy, which may result
460 from a more significant error contribution by the ground-based calculations of tree height compared to tree
461 position relative to plot center (Table 4). Both the horizontal and vertical accuracy would likely improve
462 with better SfM point clouds, which requires imagery with more overlap. Frey et al. (2018) recently found
463 that 95% overlap was preferable for generating dense point clouds, and we only achieved 91.6% overlap with
464 the X3 RGB camera and 83.9% overlap with the multispectral camera. While our live/dead classification was
465 fairly accurate (97.3% on a withheld dataset), our species classifier would likely benefit from better crown
466 segmentation because the pixel-level reflectance values within each crown are averaged to characterize the
467 “spectral signature” of each tree. With better delineation of each tree crown, the mean value of pixels within

468 each tree crown will likely be more representative of that tree's spectral signature. Better crown segmentation
469 would most readily be achieved through greater overlap in imagery. Finally, we anticipate that computer
470 vision and deep learning will prove helpful in overcoming some of these detection and classification challenges
471 (Gray et al. 2019).

472 **Conclusions**

473 Climate change adaptation strategies emphasize reducing tree densities to restore forest resilience (North et
474 al. 2015, Young et al. 2017), but understanding the optimal complex forest structure that can enable dry
475 western U.S. forests to persist through disturbances such as insect attack will be vital for predicting how
476 California forests may respond to these interventions. We've shown that drones can be a valuable tool for
477 investigating how this complexity in forest structure combines with environmental conditions to shape forest
478 insect disturbance.

479 Our results support conclusions of other researchers that management interventions to reduce the severity of
480 bark beetle disturbance will benefit from generally reducing tree density (Young et al. 2017). However, in
481 addition, our study suggests that outcomes will depend on whether the disturbance dynamic has crossed
482 endemic to outbreak feedback thresholds (Raffa et al. 2008), which may be predicted by recent advances in
483 disturbance forecasting (Preisler et al. 2017).

484 **Acknowledgements**

485 We gratefully acknowledge funding from the USDA Forest Service Western Wildlands Environmental Threat
486 Assessment Center (WWETAC) as well as Connie Millar for comments and guidance during the development
487 of this project.

488 **References**

- 489 Anderegg, W. R. L., J. A. Hicke, R. A. Fisher, C. D. Allen, J. Aukema, B. Bentz, S. Hood, J. W. Lichstein,
490 A. K. Macalady, N. McDowell, Y. Pan, K. Raffa, A. Sala, J. D. Shaw, N. L. Stephenson, C. Tague, and
491 M. Zeppel. 2015. Tree mortality from drought, insects, and their interactions in a changing climate. New
492 Phytologist 208:674–683.
- 493 Asner, G. P., P. G. Brodrick, C. B. Anderson, N. Vaughn, D. E. Knapp, and R. E. Martin. 2016. Progressive
494 forest canopy water loss during the 2012-2015 California drought. Proceedings of the National Academy of

- 495 Sciences 113:E249–E255.
- 496 Baldwin, B. G., A. H. Thornhill, W. A. Freyman, D. D. Ackerly, M. M. Kling, N. Morueta-Holme, and B. D.
497 Mishler. 2017. Species richness and endemism in the native flora of California. American Journal of Botany
498 104:487–501.
- 499 Bentz, B. J., J. Régnière, C. J. Fettig, E. M. Hansen, J. L. Hayes, J. A. Hicke, R. G. Kelsey, J. F. Negrón,
500 and S. J. Seybold. 2010. Climate change and bark beetles of the western United States and Canada: Direct
501 and indirect effects. BioScience 60:602–613.
- 502 Berryman, A. A. 1982. Population dynamics of bark beetles. Pages 264–314 in Bark Beetles in North
503 American Conifers: A System for the Study of Evolutionary Biology.
- 504 Brooks, S. P., and A. Gelman. 1998. General methods for monitoring convergence of iterative simulations.
505 Journal of Computational and Graphical Statistics 7:434.
- 506 Bürkner, P.-C. 2017. **brms**: An *R* package for bayesian multilevel models using *Stan*. Journal of Statistical
507 Software 80.
- 508 Chubaty, A. M., B. D. Roitberg, and C. Li. 2009. A dynamic host selection model for mountain pine beetle,
509 *Dendroctonus ponderosae* Hopkins. Ecological Modelling 220:1241–1250.
- 510 Clevers, J., and A. Gitelson. 2013. Remote estimation of crop and grass chlorophyll and nitrogen content using
511 red-edge bands on Sentinel-2 and -3. International Journal of Applied Earth Observation and Geoinformation
512 23:344–351.
- 513 Coops, N. C., M. Johnson, M. A. Wulder, and J. C. White. 2006. Assessment of QuickBird high spatial
514 resolution imagery to detect red attack damage due to mountain pine beetle infestation. Remote Sensing of
515 Environment 103:67–80.
- 516 DJI. 2015a. Zenmuse X3 - Creativity Unleashed. <https://www.dji.com/zenmuse-x3/info>.
- 517 DJI. 2015b. DJI - The World Leader in Camera Drones/Quadcopters for Aerial Photography. <https://www.dji.com/matrice100/info>.
- 519 DronesMadeEasy. 2018. Map Pilot for DJI on iOS. <https://itunes.apple.com/us/app/map-pilot-for-dji/id1014765000?mt=8>.
- 521 Evenden, M. L., C. M. Whitehouse, and J. Sykes. 2014. Factors influencing flight capacity of the mountain
522 pine beetle (Coleoptera: Curculionidae: Scolytinae). Environmental Entomology 43:187–196.
- 523 Eysn, L., M. Hollaus, E. Lindberg, F. Berger, J.-M. Monnet, M. Dalponte, M. Kobal, M. Pellegrini, E.

- 524 Lingua, D. Mongus, and N. Pfeifer. 2015. A benchmark of LiDAR-based single tree detection methods using
525 heterogeneous forest data from the alpine space. *Forests* 6:1721–1747.
- 526 Farr, T. G., P. A. Rosen, E. Caro, R. Crippen, R. Duren, S. Hensley, M. Kobrick, M. Paller, E. Rodriguez, L.
527 Roth, D. Seal, S. Shaffer, J. Shimada, J. Umland, M. Werner, M. Oskin, D. Burbank, and D. Alsdorf. 2007.
528 The Shuttle Radar Topography Mission. *Reviews of Geophysics* 45.
- 529 Fettig, C. J. 2012. Chapter 2: Forest health and bark beetles. *in* Managing Sierra Nevada Forests. PSW-
530 GTR-237. USDA Forest Service.
- 531 Fettig, C. J. 2016. Native bark beetles and wood borers in Mediterranean forests of California. Pages 499–528
532 *in* Insects and diseases of Mediterranean Forest systems. Springer International Publishing, Switzerland.
- 533 Fettig, C. J., K. D. Klepzig, R. F. Billings, A. S. Munson, T. E. Nebeker, J. F. Negrón, and J. T. Nowak. 2007.
534 The effectiveness of vegetation management practices for prevention and control of bark beetle infestations in
535 coniferous forests of the western and southern United States. *Forest Ecology and Management* 238:24–53.
- 536 Fettig, C. J., L. A. Mortenson, B. M. Bulaon, and P. B. Foulk. 2019. Tree mortality following drought in the
537 central and southern Sierra Nevada, California, U.S. *Forest Ecology and Management* 432:164–178.
- 538 Flint, L. E., A. L. Flint, J. H. Thorne, and R. Boynton. 2013. Fine-scale hydrologic modeling for regional land-
539 scape applications: The California Basin Characterization Model development and performance. *Ecological
540 Processes* 2:25.
- 541 Floyd, M. L., M. Clifford, N. S. Cobb, D. Hanna, R. Delph, P. Ford, and D. Turner. 2009. Relationship of
542 stand characteristics to drought-induced mortality in three Southwestern piñonJuniper woodlands. *Ecological
543 Applications* 19:1223–1230.
- 544 Franceschi, V. R., P. Krokene, E. Christiansen, and T. Krekling. 2005. Anatomical and chemical defenses of
545 conifer bark against bark beetles and other pests. *New Phytologist* 167:353–376.
- 546 Frey, J., K. Kovach, S. Stemmler, and B. Koch. 2018. UAV photogrammetry of forests as a vulnerable
547 process. A sensitivity analysis for a structure from motion RGB-image pipeline. *Remote Sensing* 10:912.
- 548 Gabry, J., D. Simpson, A. Vehtari, M. Betancourt, and A. Gelman. 2019. Visualization in Bayesian workflow.
549 *Journal of the Royal Statistical Society: Series A (Statistics in Society)* 182:389–402.
- 550 Gitelson, A., and M. N. Merzlyak. 1994. Spectral reflectance changes associated with autumn senescence
551 of *Aesculus hippocastanum* L. and *Acer platanoides* L. leaves. spectral features and relation to chlorophyll

- 552 estimation. *Journal of Plant Physiology* 143:286–292.
- 553 Graf, M., M. Reid, B. Aukema, and B. Lindgren. 2012. Association of tree diameter with body size and lipid
554 content of mountain pine beetles. *The Canadian Entomologist* 144:467–477.
- 555 Gray, P. C., A. B. Fleishman, D. J. Klein, M. W. McKown, V. S. Bézy, K. J. Lohmann, and D. W. Johnston.
556 2019. A convolutional neural network for detecting sea turtles in drone imagery. *Methods in Ecology and
557 Evolution* 10:345–355.
- 558 Griffin, D., and K. J. Anchukaitis. 2014. How unusual is the 2012-2014 California drought? *Geophysical
559 Research Letters* 41:9017–9023.
- 560 Hayes, C. J., C. J. Fettig, and L. D. Merrill. 2009. Evaluation of multiple funnel traps and stand characteristics
561 for estimating western pine beetle-caused tree mortality. *Journal of Economic Entomology* 102:2170–2182.
- 562 Hijmans, R. J., J. van Etten, M. Sumner, J. Cheng, A. Bevan, R. Bivand, L. Busetto, M. Canty, D. Forrest,
563 A. Ghosh, D. Golicher, J. Gray, J. A. Greenberg, P. Hiemstra, I. for M. A. Geosciences, C. Karney, M.
564 Mattiuzzi, S. Mosher, J. Nowosad, E. Pebesma, O. P. Lamigueiro, E. B. Racine, B. Rowlingson, A. Shortridge,
565 B. Venables, and R. Wueest. 2019. *Raster: Geographic data analysis and modeling*.
- 566 Hunziker, P. 2017. *Velox: Fast raster manipulation and extraction*.
- 567 Jakubowski, M. K., W. Li, Q. Guo, and M. Kelly. 2013. Delineating individual trees from LiDAR data: A
568 comparison of vector- and raster-based segmentation approaches. *Remote Sensing* 5:4163–4186.
- 569 Kane, V. R., M. P. North, J. A. Lutz, D. J. Churchill, S. L. Roberts, D. F. Smith, R. J. McGaughey, J. T.
570 Kane, and M. L. Brooks. 2014. Assessing fire effects on forest spatial structure using a fusion of Landsat and
571 airborne LiDAR data in Yosemite National Park. *Remote Sensing of Environment* 151:89–101.
- 572 Kolb, T. E., C. J. Fettig, M. P. Ayres, B. J. Bentz, J. A. Hicke, R. Mathiasen, J. E. Stewart, and A. S. Weed.
573 2016. Observed and anticipated impacts of drought on forest insects and diseases in the United States. *Forest
574 Ecology and Management* 380:321–334.
- 575 Kuhn, M. 2008. Building predictive models in R using the caret package. *Journal of Statistical Software*
576 28:1–26.
- 577 Larson, A. J., and D. Churchill. 2012. Tree spatial patterns in fire-frequent forests of western North America,
578 including mechanisms of pattern formation and implications for designing fuel reduction and restoration
579 treatments. *Forest Ecology and Management* 267:74–92.
- 580 Li, W., Q. Guo, M. K. Jakubowski, and M. Kelly. 2012. A new method for segmenting individual trees from

- 581 the LiDAR point cloud. Photogrammetric Engineering & Remote Sensing 78:75–84.
- 582 Logan, J. A., P. White, B. J. Bentz, and J. A. Powell. 1998. Model analysis of spatial patterns in mountain
583 pine beetle outbreaks. Theoretical Population Biology 53:236–255.
- 584 Meyer, F., and S. Beucher. 1990. Morphological segmentation. Journal of Visual Communication and Image
585 Representation 1:21–46.
- 586 Micasense. 2015. MicaSense. <https://support.micasense.com/hc/en-us/articles/215261448-RedEdge-User-Manual-PDF-Download>
- 587 Millar, C. I., R. D. Westfall, D. L. Delany, M. J. Bokach, A. L. Flint, and L. E. Flint. 2012. Forest mortality in
588 high-elevation whitebark pine (*Pinus albicaulis*) forests of eastern California, USA: Influence of environmental
589 context, bark beetles, climatic water deficit, and warming. Canadian Journal of Forest Research 42:749–765.
- 590 Miller, J. M., and F. P. Keen. 1960. Biology and control of the western pine beetle: A summary of the first
591 fifty years of research. US Department of Agriculture.
- 592 Moeck, H. A., D. L. Wood, and K. Q. Lindahl. 1981. Host selection behavior of bark beetles (Coleoptera:
593 Scolytidae) attacking *Pinus ponderosa*, with special emphasis on the western pine beetle, *Dendroctonus*
594 *brevicomis*. Journal of Chemical Ecology 7:49–83.
- 595 Morris, J. L., S. Cottrell, C. J. Fettig, W. D. Hansen, R. L. Sherriff, V. A. Carter, J. L. Clear, J. Clement, R.
596 J. DeRose, J. A. Hicke, P. E. Higuera, K. M. Mattor, A. W. R. Seddon, H. T. Seppä, J. D. Stednick, and S.
597 J. Seybold. 2017. Managing bark beetle impacts on ecosystems and society: Priority questions to motivate
598 future research. Journal of Applied Ecology 54:750–760.
- 599 North, M. P., S. L. Stephens, B. M. Collins, J. K. Agee, G. Aplet, J. F. Franklin, and P. Z. Fule. 2015.
600 Reform forest fire management. Science 349:1280–1281.
- 601 Pau, G., F. Fuchs, O. Sklyar, M. Boutros, and W. Huber. 2010. EBImage: An R package for image processing
602 with applications to cellular phenotypes. Bioinformatics 26:979–981.
- 603 Pebesma, E., R. Bivand, E. Racine, M. Sumner, I. Cook, T. Keitt, R. Lovelace, H. Wickham, J. Ooms, K.
604 Müller, and T. L. Pedersen. 2019. Sf: Simple features for R.
- 605 Pile, L. S., M. D. Meyer, R. Rojas, O. Roe, and M. T. Smith. 2019. Drought impacts and compounding
606 mortality on forest trees in the southern Sierra Nevada. Forests 10:237.
- 607 Plowright, A. 2018. ForestTools: Analyzing remotely sensed forest data.
- 608 Popescu, S. C., and R. H. Wynne. 2004. Seeing the trees in the forest: Using LiDAR and multispectral data
609 fusion with local filtering and variable window size for estimating tree height. Photogrammetric Engineering

- 610 and Remote Sensing:16.
- 611 Preisler, H. K., N. E. Grulke, Z. Heath, and S. L. Smith. 2017. Analysis and out-year forecast of beetle,
612 borer, and drought-induced tree mortality in California. Forest Ecology and Management. 399: 166-178
613 399:166–178.
- 614 R Core Team. 2018. R: A language and environment for statistical computing. R Foundation for Statistical
615 Computing, Vienna, Austria.
- 616 Raffa, K. F., and A. A. Berryman. 1983. The role of host plant resistance in the colonization behavior and
617 ecology of bark beetles (Coleoptera: Scolytidae). Ecological Monographs 53:27–49.
- 618 Raffa, K. F., and A. A. Berryman. 1987. Interacting selective pressures in conifer-bark beetle systems: A
619 basis for reciprocal adaptations? The American Naturalist 129:234–262.
- 620 Raffa, K. F., B. H. Aukema, B. J. Bentz, A. L. Carroll, J. A. Hicke, M. G. Turner, and W. H. Romme. 2008.
621 Cross-scale drivers of natural disturbances prone to anthropogenic amplification: The dynamics of bark beetle
622 eruptions. BioScience 58:501–517.
- 623 Raffa, K. F., J.-C. Grégoire, and B. Staffan Lindgren. 2015. Natural history and ecology of bark beetles.
624 Pages 1–40 in Bark Beetles. Elsevier.
- 625 Rouse, W., R. H. Haas, W. Deering, and J. A. Schell. 1973. Monitoring the vernal advancement and
626 retrogradation (green wave effect) of natural vegetation. Type II Report, Goddard Space Flight Center,
627 Greenbelt, MD, USA.
- 628 Roussel, J.-R. 2019. lidRplugins: Extra functions and algorithms for lidR package.
- 629 Roussel, J.-R., D. Auty, F. De Boissieu, and A. S. Meador. 2019. lidR: Airborne LiDAR data manipulation
630 and visualization for forestry applications.
- 631 Seidl, R., J. Müller, T. Hothorn, C. Bässler, M. Heurich, and M. Kautz. 2016. Small beetle, large-scale
632 drivers: How regional and landscape factors affect outbreaks of the European spruce bark beetle. The Journal
633 of applied ecology 53:530–540.
- 634 Shiklomanov, A. N., B. A. Bradley, K. M. Dahlin, A. M. Fox, C. M. Gough, F. M. Hoffman, E. M. Middleton,
635 S. P. Serbin, L. Smallman, and W. K. Smith. 2019. Enhancing global change experiments through integration
636 of remote-sensing techniques. Frontiers in Ecology and the Environment 0.
- 637 Shin, P., T. Sankey, M. Moore, and A. Thode. 2018. Evaluating unmanned aerial vehicle images for estimating

- 638 forest canopy fuels in a ponderosa pine stand. *Remote Sensing* 10:1266.
- 639 Stephenson, N. 1998. Actual evapotranspiration and deficit: Biologically meaningful correlates of vegetation
640 distribution across spatial scales. *Journal of Biogeography* 25:855–870.
- 641 Stephenson, N. L., A. J. Das, N. J. Ampersee, and B. M. Bulaon. 2019. Which trees die during drought?
642 The key role of insect host-tree selection. *Journal of Ecology*:75.
- 643 Thistle, H. W., H. Peterson, G. Allwine, B. Lamb, T. Strand, E. H. Holsten, and P. J. Shea. 2004. Surrogate
644 pheromone plumes in three forest trunk spaces: Composite statistics and case studies. *Forest Science* 50.
- 645 USDAFS. 2019, February 11. Press Release: Survey finds 18 million trees died in California in 2018.
646 https://www.fs.usda.gov/Internet/FSE_DOCUMENTS/FSEPRD609321.pdf.
- 647 Vega, C., A. Hamrouni, S. El Mokhtari, J. Morel, J. Bock, J. P. Renaud, M. Bouvier, and S. Durrieu. 2014.
648 PTrees: A point-based approach to forest tree extraction from LiDAR data. *International Journal of Applied
649 Earth Observation and Geoinformation* 33:98–108.
- 650 White, P., and J. Powell. 1997. Phase transition from environmental to dynamic determinism in mountain
651 pine beetle attack. *Bulletin of Mathematical Biology* 59:609–643.
- 652 Young, D. J. N., J. T. Stevens, J. M. Earles, J. Moore, A. Ellis, A. L. Jirka, and A. M. Latimer. 2017.
653 Long-term climate and competition explain forest mortality patterns under extreme drought. *Ecology Letters*
654 20:78–86.
- 655 Zhang, W., J. Qi, P. Wan, H. Wang, D. Xie, X. Wang, and G. Yan. 2016. An easy-to-use airborne LiDAR
656 data filtering method based on cloth simulation. *Remote Sensing* 8:501.